Torstein Nordvik

Dehydration and Intercalation of CO_2 in Fe-Fluorohectorites and Thermogravimetric Analysis of Cation Exchanged Fluorohectorites

Master's thesis in Nanotechnology
Supervisor: Jon Otto Fossum
June 2023

Torstein Nordvik

Dehydration and Intercalation of CO_2 in Fe-Fluorohectorites and Thermogravimetric Analysis of Cation Exchanged Fluorohectorites

Master's thesis in Nanotechnology
Supervisor: Jon Otto Fossum
June 2023

Norwegian University of Science and Technology
Faculty of Natural Sciences
Department of Physics

NTNU
Norwegian University of
Science and Technology

June 19, 2023

Preface

I am delighted to present this master's thesis, which focuses on the captivating field of CO_2 capture in clays. This research work represents a significant milestone in my academic journey and would not have been possible without the guidance, support, and expertise of numerous individuals.

First and foremost, I would like to express my sincere gratitude to my supervisor, Prof. Jon Otto Fossum. His knowledge, insightful feedback and guidance have been instrumental in shaping the direction and quality of this study. I am grateful for the opportunity to work under his supervision.

I would also like to extend my appreciation to Konstanse Kvalem Seljelid, who has graciously assumed the position as my co-supervisor. Her inputs, explanations, and valuable suggestions have significantly contributed to the development and refinement of this research.

Furthermore, I am incredibly thankful to the European Synchrotron Radiation Facility for generously providing access to their state-of-the-art synchrotron facility. This especially includes the beamline scientists at SNBL: Dimitry, Vadim and Charlie. I would like to extend my appreciation to the XRD lab at IMA for granting me access to their D8 Focus.

This master's degree thesis represents the culmination of countless hours of hard work, dedication, and collaboration. It is my sincere hope that this research will contribute to the expanding knowledge base in the field of CO_2 capture in clays.

Torstein Nordvik

Abstract

The interlayer pore space of clay minerals have shown to be a competitive adsorption material for carbon dioxide. In this report the uptake of CO_2 in two different Fe^{3+} exchanged fluorohectorite (Fe(III)-FHT & Fe(III)-FHT-sim) has been studied. Dried Fe(III)-FHT showed a swelling at 18 bar of CO_2. Both increased pressure and high pressure over time resulted in increased swelling. The swelling was largest at 50 bar for different pressure steps: 0.48 Å thicker interlayer compared to dry Fe(III)-FHT, which has a d-spacing of 10.74 Å. High pressurized sample gave a swelling of 0.55 Å after 3 hours for Fe(III)-FHT-sim. The swelling is related to CO_2 adsorption in the interlayer, where iron hydroxides works as adsorptions sites. After exposure, the CO_2 stayed in the interlayer for low pressures and desorbed only when the fluorohectorite was heated. The intercalation was reversible and CO_2 was fully removed from the clay at 423 K.

Thermogravimetric analysis showed a water amount between 6.7-16.2% and the possibility of dehydroxylation for intercalated hydroxides. The dried samples did not show water uptake upon cooling above 323 K. Additionally, the more amorphous samples of dried Fe(III)-FHT showed an increased ability for water uptake at 298 K.

Sammendrag

Karbonfangst i leire er blitt undersøkt som et resultat av økende CO_2 i atmosfæren. CO_2 kan absorberes i leire [1] og i denne oppgaven er denne absorpsjon undersøkt for prøvene Fe(III)-FHT og Fe(III)-FHT-sim, som er fluor-hektoritt med forskjellig protokoll for kation utbytting av Fe^{3+}.
Målinger ved ESRF med røntgendiffraksjon viste at Fe(III)-FHT hadde et CO_2-opptak som tilsvarer en utvidelse på 0.47 Å mellom leirelagene ved 50 bar. Tørr Fe(III)-FHT har en basal avstand på 10.74 Å. Opptaket av CO_2 startet ved 18 bar og fulgte en hysterese kurve som tilsier at CO_2 har vanskeligheter for å gå ut av leiren når den først er tatt opp. Oppvarming til 423 K førte leirelagene tilbake til en avstand tilsvarende tørr prøve. Fe(III)-FHT-sim ga et utvidelse på 0.55 Å etter 3 timer ved 40 bar CO_2. Dette viser at opptaket av leire også kan være veldig langsomt og vankelig å oppdage. Dette er i kontrast til Fe(III)-FHT, hvor absorpsjonen er demonstrert til å være hurtig ($\sim$ min). Begge prøvene viste at CO_2 ikke blir tatt opp mellom alle leirelagene, men kun delvis tatt opp.

CO_2-opptak i leire er forskjellig ved tilstedeværelse av vann [2]. Derfor har TGA målinger av tørkingen av Fe(III)-FHT, Fe(II & III)-FHT -sim & -pre, Cu-FHT, Mg-FHT, Zn-FHT, Mn-FHT and Ni-FHT blitt undersøkt. Prøvene har mellom 6.7-16.2% vann og et vannlag rundt hydroksidet ved en luftfuktighet på 43%. Det varierer fra prøve til prøve om hydroksidet mellom leirelagene brytes ned ved den forventede temperaturen. FHT prøver med jernhydroksid viser seg å tørke ved 423 K og for å tørke mellom leirelagene må også vakuum settes på prøvene.

Contents

Figures

Tables

1 Introduction

Clay is a versatile material that extends beyond its traditional use in ceramics. Its applications span various industries, including cosmetics, nuclear waste storage, and paints, among others [3, 4]. With its wide-ranging uses and extensive research, clay holds great potential for driving new technologies in the future.

One intriguing characteristic of clay is its high effective surface area [5]. Combining this property with an adsorption mechanism can yield significant benefits. A particularly relevant and contemporary application is, for example, the possibility for adsorption of carbon dioxide through post-combustion sequestration.

The pressing challenges posed by climate change call for urgent technological solutions. Concentrations of carbon dioxide, methane and nitrous oxide reached record highs in 2021 and the globally averaged surface mole fractions are respectilvelly 149%, 262% and 124% of pre-industrial (1750) levels [6]. CO_2 is the driving force for global warming [7]. The sea level are 99 ($\pm$ 4.0) mm higher than in 1993 and is caused by thermal expansion of water and added water from melting ice sheets and glaciers [8]. Consequences related to the global warming includes reduced amount of available fresh water [9], more extreme weather [10] and widespread extinctions of species due to rapid environmental changes [11]. Carbon capturing is a crucial solution in the fight against climate change due to its ability to reduce greenhouse gas emissions [7]. By capturing carbon dioxide from industrial processes and power plants, it prevents the release of this potent greenhouse gas into the atmosphere. This technology not only helps mitigate the impact of existing emissions but also paves the way for the development of a low-carbon future by enabling the safe storage or utilization of captured carbon. By harnessing the carbon capturing capabilities of clay, it becomes possible to mitigate the greenhouse gas footprint, for instance, in the production of blue hydrogen.

Former studies have shown promising result for a reusable carbon capture process with clay material. Hemmer et al. and Michels et al. found that CO_2 intercalates in the interlayer of fluorohectorite cation exchanged with Na^+ (Na-FHT) [12, 13]. Michels et al. also found that Li-FHT and Ni-FHT have intercalation of CO_2 and that Li-FHT releases CO_2 when heated above 308 K [13]. More recent studies (2020 & 2023) by K. Hunvik et al. have

shown that dried fluorohectorite (FHT) exchanged with Ni^+ or Li^+ adsorbs CO_2 in the clay interlayer [2, 14]. Additionally, dried FHT exchanged with Na^+ (Na-FHT) did not swell, which is in contrast to wet Na-FHT.

The end goal for clay as a carbon capturing method is to utilize natural occurring clays. Mendel et al. have shown that Wyoming montmorillonite have adsorption and desorption of CO_2 in the interlayer with cation exchanged Cs^+ [15]. However, the study about natural clays is beyond the scope of this thesis.

In summary, clay's diverse applications, coupled with its high effective surface area, offer a promising way for addressing the climate challenges. The utilization of clay for carbon capture represents a modern and impactful approach that can pave the way for a more sustainable future.

In this thesis, different dried synthetic clay minerals, fluorohectorites, is investigated through X-ray diffraction experiments to find possible new interlayer cations that swell in response to CO_2. The presence of water may alter the adsorption process [2] and therefore the samples have also been investigated with thermogravimetric analysis to better understand how to remove water. This master's thesis is a continuation of a in-depth study by the author and the sections 2.1 (partly), 2.2, 3.1.1, 4.1.1 (excluding Fe(III)-FHT-sim results), 5.1.1 and 5.1.3 were also included in that study [16].

2 Theory

The theory first introduce important terms and concept to better understand X-ray diffraction. This is followed by the structure of flourohectorite clay and the interaction between water and clay, as well as CO_2 and clay. Lastly, thermogravimetric analysis is explained with an emphasis on the interaction between water and clay.

2.1 X-ray Diffraction

17 years after W.C. Röntgen discovered X-rays, the first X-ray diffraction in crystals was conducted by Max von Laue [17, 18]. At that time, X-rays had already contributed to the discovery of electrons [19] and radiotherapy [20]. X-rays diffraction turned out to be a powerful tool for studying crystals. The most important features of X-ray diffraction is that it is nondestructive and can provide information about the structure, phases, strain, texture and crystallinity of the crystalline material [21]. The characterization could be very shortly be explained as: X-rays that are scattered of a material could produces X-ray diffraction peaks due to the periodic atomic arrangements. These diffraction peaks are the 'fingerprint' of the material.

2.1.1 Miller index and crystal lattice

A crystal is formed when every lattice point has an identical basis composed of a given amount of atoms. The position of each atom is given by, $r_j = x_j a_1 + y_j a_2 + z_j a_3$ where a_1, a_2 and a_3 are the crystal axes and $j=$ 1,2,...,#atoms in basis. This is done in such a way that when viewed from a point **r**, it is identical as viewed from a point **r'**, that is translated by any of the vector **a**: **r'**=**r**+u**a**$_1$+v**a**$_2$+w**a**$_3$, where u, v and w are arbitrary integers.

The Miller indices are a notation system for different lattice planes. The three integers h, k and l determine the orientation of a crystal plane or a set of parallel planes, denoted (hkl). The vector [hkl] is perpendicular to the crystal plane (hkl) in cubic crystals. The (001) plane is shown in Figure 1.

2.1.2 Reciprocal space

Reciprocal space is an imaginary space where all lenghts are inverse of their length in real space and the different planes of atoms in real space are points in reciprocal space [22]. The reciprocal axis vectors can be expressed
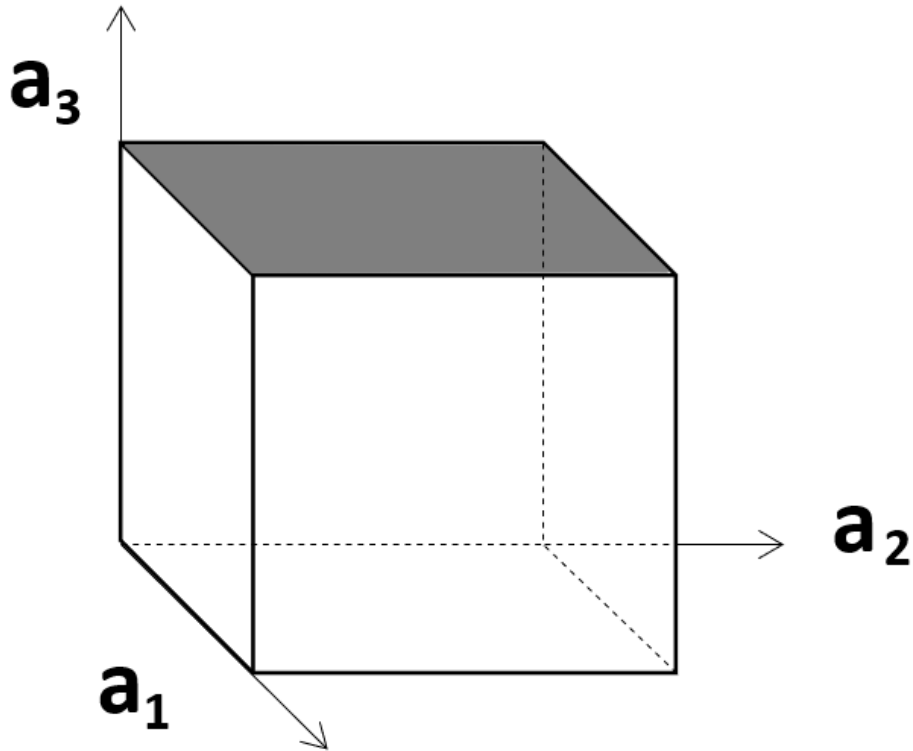
Figure 1: The Figure shows the (001) crystal plane (grey) with $\mathbf{a_1}$, $\mathbf{a_2}$ and $\mathbf{a_3}$ as the translation vectors of real space lattice of the crystal.

through the real lattice vectors,

$$\boldsymbol{b_1} = 2\pi \frac{\boldsymbol{a_2} \times \boldsymbol{a_3}}{\boldsymbol{a_1} \cdot \boldsymbol{a_2} \times \boldsymbol{a_3}}; \quad \boldsymbol{b_2} = 2\pi \frac{\boldsymbol{a_3} \times \boldsymbol{a_1}}{\boldsymbol{a_1} \cdot \boldsymbol{a_2} \times \boldsymbol{a_3}}; \quad \boldsymbol{b_3} = 2\pi \frac{\boldsymbol{a_1} \times \boldsymbol{a_2}}{\boldsymbol{a_1} \cdot \boldsymbol{a_2} \times \boldsymbol{a_3}}. \quad (1)$$

Similar too real space the different points in reciprocal space can be expressed by the set of vectors $\boldsymbol{G} = u\boldsymbol{b_1} + v\boldsymbol{b_2} + w\boldsymbol{b_3}$, where u, v and w are integers. **G** is the reciprocal lattice vector.

2.1.3 Bragg's law

Bragg's law explains the observed diffraction with the assumption that incoming waves reflects specular from parallell crystal plane. As the incoming beam propagates through the sample, only a portion of the incoming wave will scatter from each crystal plane. The difference in path length for the outgoing waves must equal to an integer number of the wavelength,

thus giving constructive interference. This is expressed through Bragg's law,

$$2d \sin\theta = n\lambda, \tag{2}$$

where θ is the angle between the incident wave and the crystal plane, λ is the wavelength of the incident wave, d is the distance between parallel planes, and n is a positive integer.

2.1.4 Laue condition

Bragg's law is only a special case of Laue diffraction, where the scattering vector is equal to the reciprocal lattice vector. The Laue condition is given by,

$$\Delta \boldsymbol{q} = \boldsymbol{G}, \tag{3}$$

Where $\boldsymbol{G}$ is a reciprocal lattice vector and $\Delta \boldsymbol{q} = \boldsymbol{q}' - \boldsymbol{q}$ the scattering vector [22]. The scattering is elastic, so the norm of the incoming and outgoing wave vector are equal. The condition in 2 dimensions is shown visually in Figure 2. The sphere is the Ewald sphere with a radius equal to the length $(2\pi/\lambda)$ of the wavevector **q**. An outgoing beam will be formed if the sphere intersect another point of the reciprocal lattice, the angle is 2θ.

2.1.5 Powder X-ray diffraction

Wide angle X-ray diffraction (WAXS) of powder is a variation of X-ray diffraction (XRD). The diffraction is more frequent in powder as the different crystal planes are oriented in all directions. The general instrument consist of three main parts as depicted in Figure 3: Detector, specimen and X-ray source. The incident wave scatters of the sample and the diffraction pattern is measured by the detector. The results from Bragg's laws and Laue condition make it possible to determine the lattice spacing.

The d-spacing is the interplanar spacing, also denoted d_{hkl}. It is inversely proportional to the norm of the reciprocal lattice vector $\boldsymbol{G}$, expressed as,

$$d_{hkl} = \frac{2\pi}{|\boldsymbol{G}|} = \frac{a}{\sqrt{h^2 + k^2 + l^2}} \tag{4}$$

for a cubic crystal [22]. Where the hkl are the Miller indices and a is the atomic spacing. This is derived from the Laue conditions. The scattered
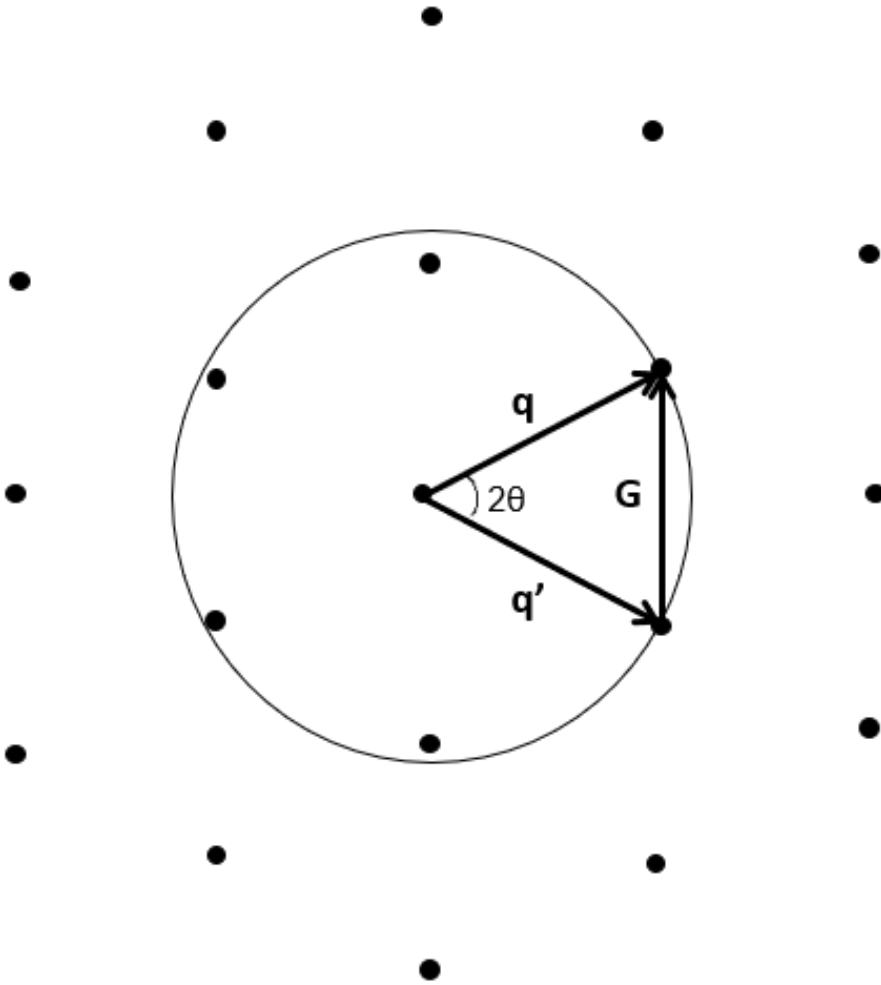
Figure 2: A 2 dimensional Ewald sphere in reciprocal space with incoming **q** and outgoing **q'** wavevectors with the angle 2θ between them. **G** is the reciprocal lattice vector.

intensity is proportional to the absolute square of the structure factor. The structure factor is expressed as,

$$S_{\boldsymbol{G}} = \sum_j f_j e^{-i\boldsymbol{r}_j \cdot \boldsymbol{G}}, \tag{5}$$

where f_j denotes the atomic form factor and $\boldsymbol{r}_j$ the relative position to the center of the j-th atom [22]. The atomic form factor is the scattering caused by the individual atom in the unit cell. This is mostly determined by the electron density for X-ray, as can be seen from the definition of atomic

Figure 3: Experimental setup of the X-ray powder diffraction. An X-ray source emits photons with wave vector $\boldsymbol{k}$, which scatter off the sample. The diffracted beam $\boldsymbol{k'}$ of angle 2θ is observed by the detector, with $\boldsymbol{\Delta k}$ being the scattering vector.

form factor,

$$f_j = \int n_j(\boldsymbol{\rho}) \exp(-i\boldsymbol{G} \cdot \boldsymbol{\rho}) \, dV, \tag{6}$$
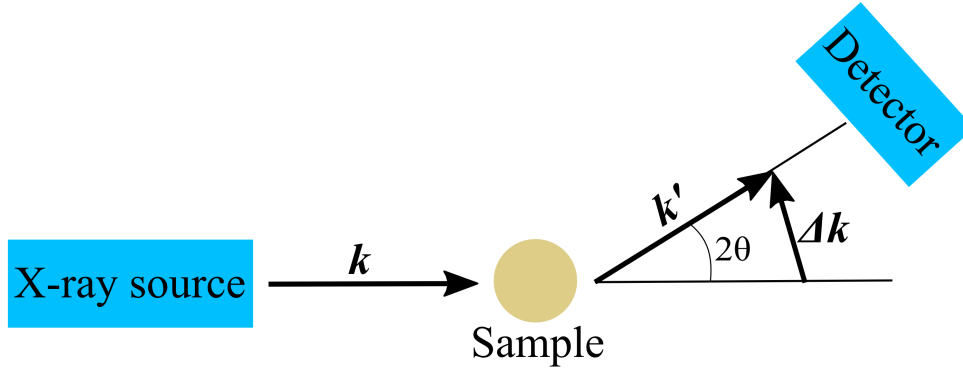
where $n_j(\boldsymbol{\rho})$ is the contribution of atom j to the electron concentration at $\boldsymbol{r}$ [22]. $\boldsymbol{\rho}$ is thus defined as $\boldsymbol{\rho} = \boldsymbol{r} - \boldsymbol{r}_j$. Because the scattering is caused by electrons, the X-rays will be sensitive to the atomic number of the atom.

2.2 Clay

Clay minerals are composed of a sheet-like structure, as seen in Figure 4. Each crystalline sheet usually consist of either an octahedral (brown layer) or a tetrahedral layer (blue layer). Both the octahedral and tetrahedral can be occupied by many different cations, where Al^{3+} is most common for octahedral and Si^{4+} for tetrahedral. The tetrahedron has four oxygen atoms coordinated to the cation. Oxygen (red atoms) can also connect the tetrahedral and octahedral layers . The octahedral layer form a hexagonal symmetry around the cation [23].

The different number and compositions of these layers is what distinguish the different clay groups and are denoted (#tetrahedral sheets: #octrahedral sheets). For example will 1:1 indicate that each clay sheet consists of one tetrahedral and one octrahedral sheet. The octrahedral sheet has three coordinated positions. If two or three of these positions are occupied, the clay is called dioctrahedral or trioctrahedral, respectively. Elements of different valence can replace aluminum or silicon as cation, this
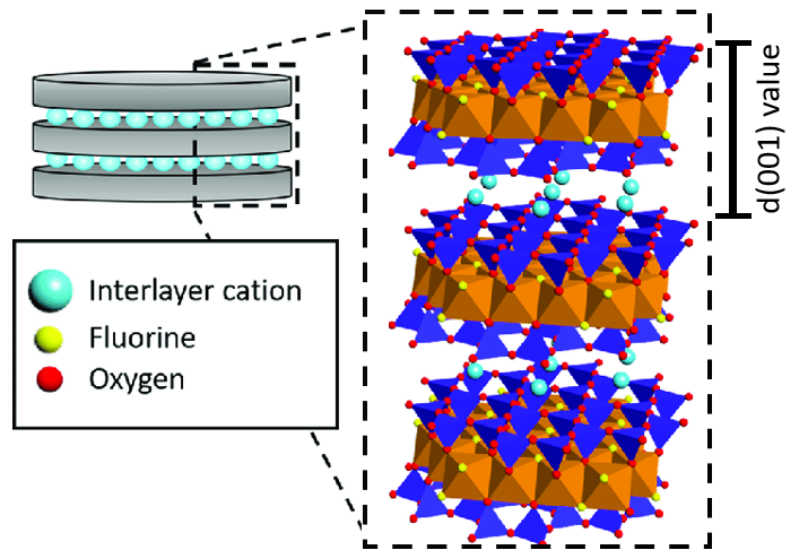
Figure 4: Structure of FHT with 2:1 structured layers with two tetrahed-ral sheets(blue), one octrahedral sheet (brown) and the interlayer cation (turquoise). The spacial part which give the 001 bragg peak is shown at the right top corner. Adapted from [24].

leads to a permanent charge on the sheet. Naturally existing clays often have sheets with negative charge, which means the substituted element is of a lower valence. Consequently, cations is located in the interlayer (tur-qouise atoms).

These interlayer-charge-compensating cations are mobile and therefore ex-changeable with other cations. The charge-compensating cations can also be located inside the crystalline layers, this is less common for naturally ex-isting clays and will not be exchangeable with other cations. In smectites, the cations effects the physicochemical behavior such as water adsorption, water retention and swelling.
Clay can be divided into two classes: swelling and non-swelling clay min-erals. Incorporated water in the crystal structure is called water of hydra-tion. Removing it can cause the clay to recrystallize into a ceramic, which is probably the oldest and most known application of clay. One layer of water between sheets is stable, but multiple layers of water can either lose or gain layers of hydration. This will cause the clay to expand or contract and is reffered to as swelling clays [25]. Non-swelling clays have no excess water layers and the sheets are compressed. There are also a possibillity for

a combination of both swelling and non-swelling layers, called mixed-layer clay.

2.2.1 Fluorohectorite, a synthetic smectite

Fluorohectorite (FHT) is a smectite 2:1 clay, where the octahedral sheet is sandwiched between two tetrahedral sheets. Smectites usually have charge per half unit cell (pfu) between 0.2 and 0.6 [23]. The cations are hydrated and are exchangeable, which mean they can be exchanged by almost any other charged atom or molecule. The measure of how easily this exchange occur is referred to as the cation exchange capacity (CEC) and is the amount of positive charge per mass in dry clay.

Since FHT is a trioctrahedral smectite it is classified as a hectorite. For smectites there are octahedral anions coordinated to the apical oxygen. These anions are usually OH^-, but for natural hectorite F^- are also present and the relative amount between them can vary. However, for synthetic fluorohectorite all the anions are fluorine.

The unit cell chemical formula for FHT is $M_x(Mg_{6-x}Li_x)Si_8O_{20}F_4$, where x is the charge per formula unit and is depicted with an arbitrary exchange cation M in Figure 4 [26]. The FHT particles have 10 Å thick platelets, stacked with the height of approximately 100 nm and between 200 nm and 2 μm wide. FHT is used instead of natural smectite because it contains fewer impurities and has more homogeneous charge distribution.

This is an advantage as the cation exchange can be a selective process, where larger inorganic cations are preferred over small ones. Smectites are highly interesting due to reactions that can take place in the interlayer space. Both polar and non-polar species can interact with the interlayer hydrated cation.

2.2.2 Water in the interlayer

Water is present in a variaty of states in clay minerals: free water, structural hydroxyl groups, interlayer water, and water molecules adsorbed on clay surfaces. In order to understand the interaction between CO_2 and clay, the interaction of water and clay has to be explored. The most important interaction is between water and the exchangeable cation in the interlayer. When cations react with water the hydroxide ion ($-OH$) bind to the cation and form a cation-hydroxide. This cation hydroxide is usually referred to as the interlayer cation. Further reaction with water is the hydration of the cation and is controlled by the size and morhology of the clay particle, hydration energy of the cation and difference in electrostatic surface potential as a consequence of the different locations of layer charges. The two

types of hydration will be presented:

(i) *Inner sphere complex*
Cations with a strong polarizing power tend to form stronger hydrogen bonds with water molecules. Consequently, cations with stronger polarizing power can promote more water adsorption [27]. The first type of hydration is when the cation is bound to the water molecules, in an inner sphere complex, and the clay surface . This is referred to as a water layer (WL) and will give an increase in the d-spacing of the clay. A typical increase of about 2.5 Å can be seen as 1 WL goes into the interlayer of the clay.

(ii) *outer sphere complex*
The polarizing power will effect the strength of the hydrogen bond for a possible second WL to attach on the outer coordination sphere. The hydration of the cation is controlled by electrostatic interaction. Minimization of the water-water repulsion and a maximal charge-dipole attraction will facilite for two and three WL. Here the cation only interacts with the water molecules and form water ligands.

In addition to the high polarizing power or hydration energy of the cation, the humidity must also increase. When the humidity is high enough the 2. and 3. WL can form and discrete crystalline swelling occurs. Further increasing the humidity leads to osmotic swelling and the layers will delaminate.

Na^+ and Li^+ has a high enough hydration energy and swell with response to water vapor (0-2WL). Cations with lower hydration energy, such as K^+ and Rb^+, did not give swelling in response to water vapor. However, Cs^+ with an even lower hydration energy than previous mentioned cations, did show swelling of 1 WL. The swelling in Cs-FHT was attributed to the large radius of the Cs^+ ion [28].

The interaction is weaker for higher temperatures and can dehydrate the clay at sufficient temperatures. When water from outer coordination sphere is removed, the water molecules(from 1 WL) and surface oxygen of the clay layer form a coordination.

To summarize, the clay interlayer can either have 0,1,2 or 3 WL, each of which cause a swelling in d-spacing of the clay interlayer. This is effected by both the hydration energy and the radius of the interlayer cation.

2.2.3 Intercalation of CO_2 in clay

The water and CO_2 competes for active surface sites, but the adsorption of CO_2 is also observed to decrease with decreasing humidity. Figure 5 shows the difference in swelling for montmorillonite and hectorite under pressurized CO_2 gas with different numbers of WL [1].
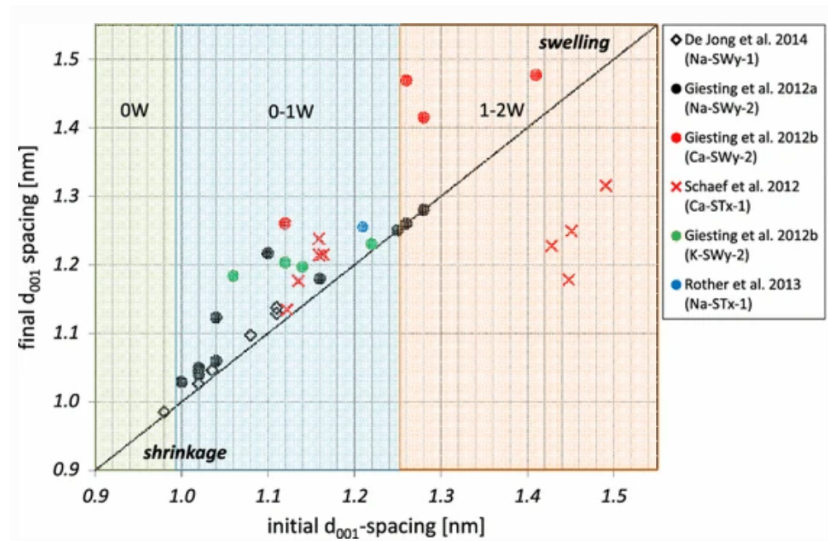
Figure 5: Summary of maximum smectite interlayer spacing d_{001} after charging samples with CO_2. Hydration states (0 WL, 1 WL etc.) relate to interlayer water layers. These depend on the interlayer cation, on relative humidity, temperature and pressure (in this case only hydrostatic). Between the three hydration fields indicated in the figure are discrete states with almost all of the clay minerals having the same hydration state (either 1 WL or 2 WL). Two different clays were used: Wyoming and Texas MMT. Adapted with permission from [1]

For 0 WL there is little swelling. The swelling increases for higher hydration as now a combination of 0 and 1 WL will be present in the clay. When all interlayers reach 1 WL the swelling does not increase as much and for 2 WL there is a shrink and the clay dehydrate by the surrounding CO_2 [1].

Intercalation is when ions or molecules are adsorbed into the interlayer of a clay. The intercalation can sometimes even be irreversible. The adsorption of CO_2 is dependent on the initial hydration, type of clay and interlayer cation. The cation exchange effects the availability of clay surface. This happens first at edge sites and the outer layer surfaces aggregate before affecting interlamellar sites. Cations with a high valence can bind the edges of the clay together and larger aggregates form. This leads to less external surface area.

The process of intercalation of CO_2 is complex and not entirely understood and as Table 1 shows, H_2O and CO_2 have different physical properties. Unlike water, CO_2 is not polar and the underlying molecular mechanism needs more understanding.

Table 1: Physical properties of H_2O and CO_2.

molecule	Kinetic diameter (Å)	Dipole moment (D)
H_2O	2.65	1.85
CO_2	3.30	0

Hunvik et al. report that the uptake of CO_2 in the interlayer will increase when the clay layer charge decreases [5]. The interlayer cations have different sizes and valency and therefore different potential to polarize the CO_2 molecule and still form hydroxides with the chosen cation. Table 2 shows the hydration energy of relevant cations.

Table 2: Physical parameters of the included cations [29], [30]

| Element	Ionic radius (Å)	Hydration energy (kJ/mol)	Ion charge
Fe	0.65	-4429	+3
Fe	0.78	-1946	+2
Zn	0.74	-2047	+2
Mg	0.72	-1926	+2
Cu	0.73	-2099	+2
Mn	0.83	-1851	+2
Ni	0.69	-2096	+2

2.3 Thermogravimetric Analysis

Thermogravimetric analysis (TGA) is a measure of the mass of a substance as a function of time or temperature [31]. Typically the technique consist of a weighing balance, a cooling/heating system, a gas inlet/outlet and a data representation system. The different causes for weight loss during heating is usually:

- Evaporation - volatile substances evaporate at different temperatures
- Thermal decomposition - chemical compounds break down
- Reduction - loss of oxygen
- Desorption - of adsorbed substances

Oppositely, weight gain can be caused by oxidation and absorption. The weight of a sample is measured upon heating and this is referred to as a thermogram or TGA curve. Since all weight gain/loss processes are kinetic there is a rate at which they occur and the first derivative of the TGA curve is referred to as the DTG curve.

Calibration of TGA are normally checked with either a melting point standard or the magnetic transition of ferromagnetic materials. A third option is possible with the use of calcium oxalate monohydrate (kidney stone), because it undergoes three distinct weight losses [32], as shown in the following chemical reactions.

$$CaC_2O_4 \cdot H_2O\,(s) \rightarrow CaC_2O_4\,(s) + H_2O\,(g), \qquad (7)$$
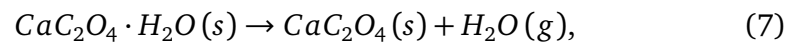
The first step is evaporation of water and occurs at approximately 453 K [32].

$$CaC_2O_4\,(s) \rightarrow CaCO_3\,(s) + CO\,(g), \qquad (8)$$
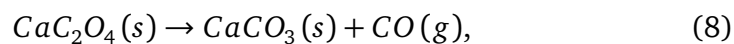
Calcium oxalate thermally decomposes to calcium carbonate and carbon monoxide at approximately 773 K [32].

$$CaCO_3\,(s) \rightarrow CaO\,(s) + CO_2\,(g), \qquad (9)$$
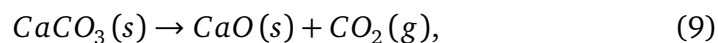
and at approximately 1023 K, with the loss of CO_2, calcium carbonate thermally decompose to calcium oxide[32]. The theoretical amount of weight loss for each step is 12.3%, 19.2% and 30.1%, respectively.

2.3.1 Water evaporation and dehydroxilation

A wet FHT clay samples will show a decrease in weight when heated because the water evaporates. A previous study by Loch et al. has shown a weight reduction for Ni-FHT and Na-FHT of 13.8% and 9.9%, respectively

[33]. The reported weightloss for Ni-FHT before dehydroxylation was explained by the loss of interlayer and coordinated water. This compared well to the theoretical weight loss of 2 WL. The Na-FHT dehydration occured between 363-393 K and the theoretical weight loss was attributed to the dehydration of 1 WL. The thermal behavior of Ni-FHT showed to be more complex than Na-FHT and at 640 K another weight reduction of around 3% was observed. The weight reduction was assigned to a dehydroxilation of β-Ni(OH)$_2$ to NiO and compare well to the expected weight loss of a dehydroxylation process (approximately 3-4%). For Na-FHT only dehydration was observed and no dehydroxilation.

Table 3 shows the theoretical calculated mass loss of coordinated water for the flourohectorite samples. Fe(III)-FHT samples was separated from the rest as it has a vacancy of 3+ and therefore have an extra OH-group in the hydroxides. The suffixes -pre and -sim refer to the order in which the cation salt solution (for cation exchange) was added in relation to the water and clay solution. 'Pre' indicates that the clay and water were mixed 24 h before the salt solution was added, while 'sim' indicates that the clay, water, and salt solution were mixed simultaneously.

Table 3: Theoretical calculated mass loss for the different clay samples for 1 WL, 2 WL and dehydroxylation process, calculated from an initial state of either 2 WL or 1 WL. Mg-FHT, Cu-FHT, Mn-FHT, Ni-FHT, Zn-FHT, Fe(II)-FHT-sim and Fe(II)-FHT-pre have been given a mass loss interval, due too similar values.

Sample	initial state	Mass loss (%)		
		Outer WL	Inner WL	Dehydroxilation
Fe(III)-FHT, Fe(III)-FHT-pre, and Fe(III)-FHT-sim	2 WL	6.2	6.9	4.9
	1 WL	-	7.4	5.3
Mg-FHT, Cu-FHT, Mn-FHT, Ni-FHT, Zn-FHT, Fe(II)-FHT-sim, and Fe(II)-FHT-pre	2 WL	6.3-6.8	7.0-7.6	3.3-3.6
	1 WL	-	7.5-8.1	3.6-3.7

Table 4 shows the temperatures at where the cation hydroxides dehydroxilates and is reffered to as the decomposition temperature T_d. This temperature has shown to depend on crystal size, crystallinity and pH during the synthesis of Ni(OH)$_2$ [34]. The T_d of cation hydroxides inside the

FHT samples can therefore vary from the reported T_d from Table 4, which are for solid cation hydroxides.

Table 4: Decomposition temperatures (T_d) of Fe(III), Fe(II), Zn, Mg, Cu and Ni. These values are for free cation hydroxides and not for interlayer cations in flourohectorite [30, 35–37]. The decomposition temperature of Ni as an interlayer cation of FHT is put in the parenthesis [33].

Cation	T_d (K)	T_d (C)
Fe(III)	773	500
Fe(II)	< 473	< 200
Zn	398	125
Mg	653	380
Cu	423	150
Mn	-	-
Ni	503	230 (200-300)

3 Method

Thermogravimetric analysis (TGA) was employed to investigate the interaction between clay and water, while X-ray diffraction (XRD) measurements were utilized to study the interaction between CO2 and clay. By employing these complementary techniques, a comprehensive understanding of the interaction of flourohectorite with both water and CO2 was aimed to be achieved.

3.1 XRD

3.1.1 European Synchrotron Radiation Facility

The Swiss-Norwegian beamline (BM01) at ESRF in Grenoble, France, was used for the measurement of the samples. The monochromatic beam from a Si(111) double-crystal had a wavelength of $\lambda = 0.60546$ Å and beam cross-section of 0.2mm × 0.2mm. A protective sheet of Kapton was placed in front of the PILATUS2M detector. LaB_6 sample was used for calibration

Each sample was pulverized and put in a glass capillary with a dimension of 0.5mm. The capillary was glued to a Swagelok weld gland with UV-curable glue for long term seal that can hold high pressure and vacuum. The samples were all dehydrated with high vacuum at 423 K. Glasswool was inserted in the capillary to prevent the powder from being sucked out by the vacuum. The temperature was controlled by a cryostream (N_2 gas). If the sample was considered dry the temperature was brought down to 300 K for verification. The criteria for a dry sample was that the peak position was unchanged during and after cooling. Narrowing of the peak could occur since the clay sheets in general get straighter for lower temperature. If the sample was either wet or had a smaller d-spacing than 10 Å, the sample was not pressurized with CO_2. The powder was exposed to step-wise CO_2 pressures and lastly heated to possibly reverse any intercalation. The sample was rotated 30 degrees for each measurement to increase the statistics of the powder scattering. The Fe(III)-FHT-sim were only exposed to 40 bar CO_2 for 3 hours after drying, with a rotation of 10 degrees.

The recorded diffractogram from the synchrotron is two-dimensional and therefore azimuthally averaged over. The resulting data are presented as intensity vs scattering vector, shown in Figure 6.
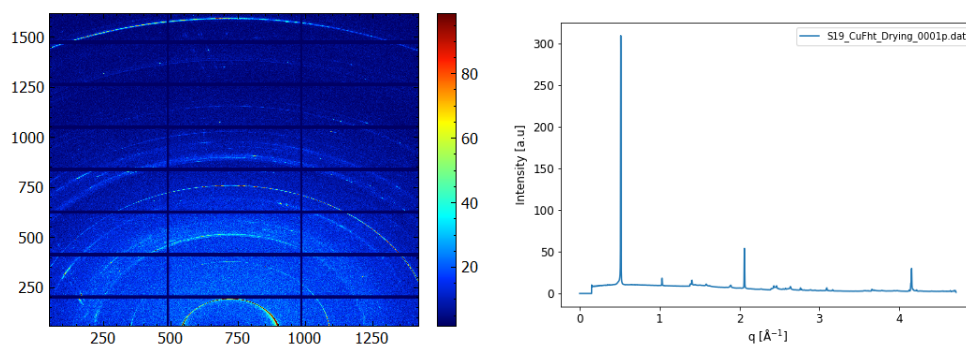
(a) Diffractogram data as detected at the beamline.

(b) Azimuthally integrated diffractogram of Cu-FHT (I vs q).

Figure 6: Data from ESRF for Cu-FHT

3.1.2 D8 Focus

The D8 Focus, seen in Figure 7, had CuKα radiation with a wavelength of 1.54 Å and a LynxEye SuperSpeed Detector. The D8 Focus was used to confirm the results from ESRF.

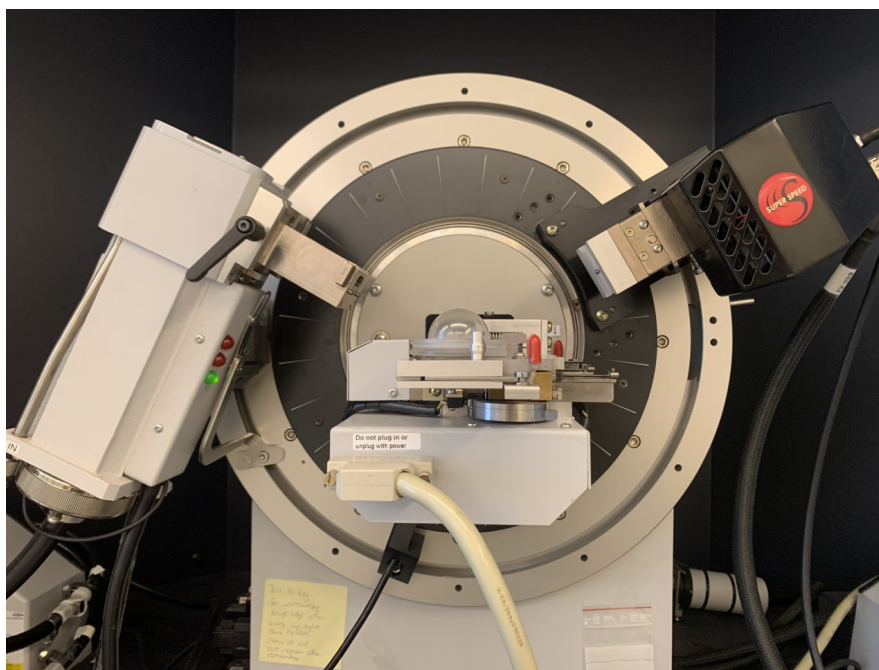**Figure 7:** Overview picture of the D8 Focus with inserted domeholder between the source (left) and the detector (right).

The Fe(III & II)-FHT,-sim & -pre powder was either dried or hydrated and then placed in a 10 mm Si-cavity and sealed with an airtight dome holder as shown on Figure 8. The wet Fe(III & II)-FHT,-sim & -pre was put in a desiccator with saturated potassium carbonate to achieve an atmosphere of 43% relative humidity (RH). The samples were exposed to 43% RH for 24 hours and for the drying process the powder dried at 423 K for 24 hours in a glovebox with N_2-gas and an atmosphere with 3% RH. All samples were measured at an angle 2θ from 3 to 60 degrees with a 0.1 mm slit opening.
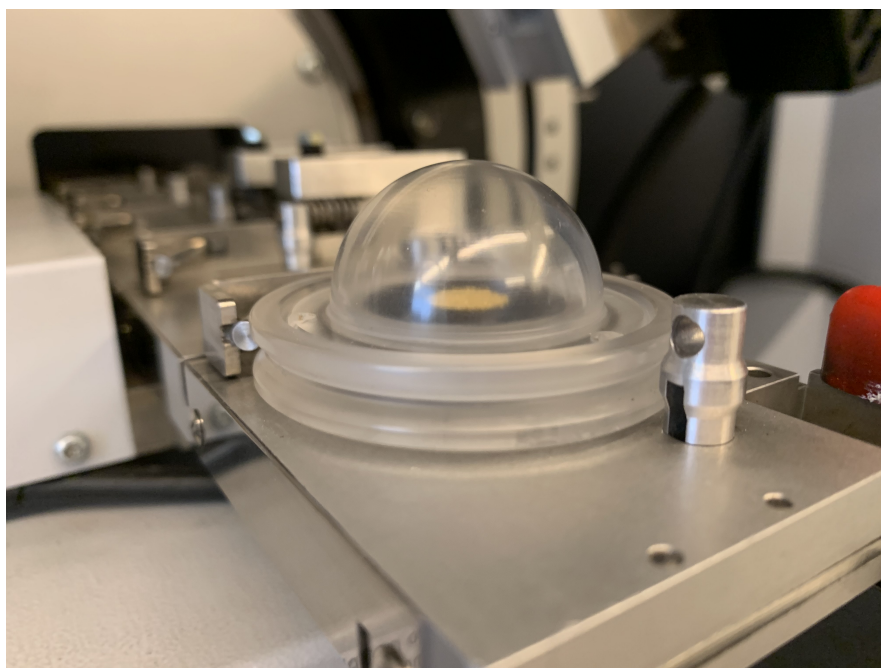

Figure 8: 10 mm Si insert with a surrounding airtight domeholder in the sample holder of the D8 Focus.

3.2 TGA

TGA/SDTA851e/LF/1100 model with TGA/LF SDTA FRS1 sensor was used for the TGA measurements. Figure 9 shows the weighing balance and the 70 μL aluminum oxide crucible with a lid.

The software used for temperature, time steps and weight measurement was STARe SW 16.20. The software had limitations of a maximum of 60 000 measurement with a prefixed setting of 1 measurement per second. Therefore each measurement could not be longer than approximately 16.6 hours. Additionally, there could only be a total of 10 isothermal
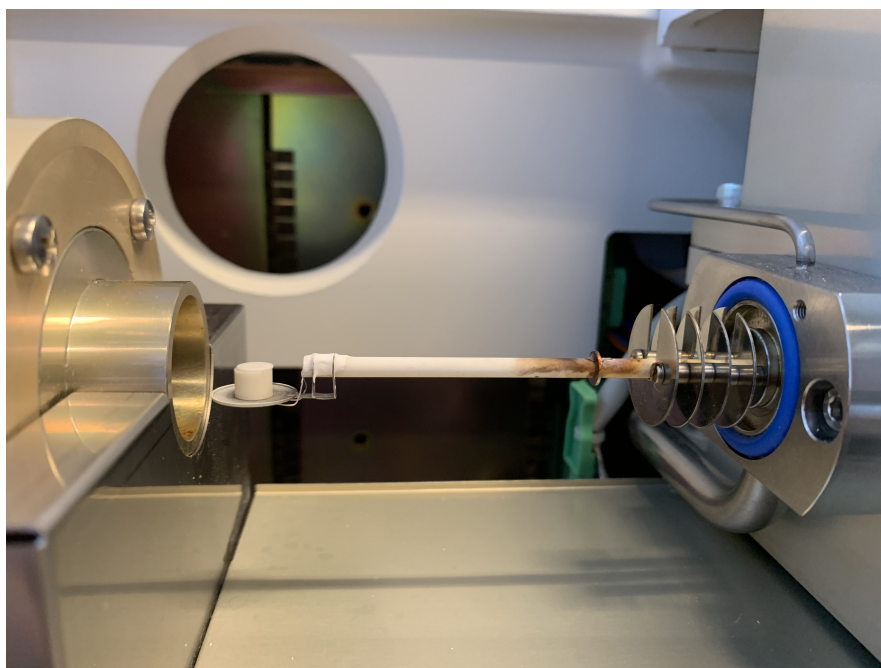
Figure 9: Weighing balance of the TGA/SDTA851e/LF/1100 with the 70 μL aluminum oxide crucible with a lid.

and thermally dynamic steps. The calibration was done with calcium oxalate monohydrate (See Appendix A).

As discussed in section 2.2.2, the interaction between clay and water is highly dependent on the interlayer cation. In order to separate swelling caused by H_2O and CO_2 with higher accuracy, the temperature at which water leaves and enters the clay is investigated. The moisture content of the material could be measured through the weight difference. The assumption for the TGA measurement is that only water molecules evaporates from the different clay samples below a temperature of 573 K.

The first drying processes were conducted to understand the time it takes to dry a sample and whether or not water returns to the sample upon cooling. Fe(III)-FHT, Cu-FHT, Mg-FHT, Zn-FHT, Mn-FHT and Ni-FHT powder were put in an aluminum oxide crucible with a lid and evenly distributed. The starting weight of each sample were measured with OHAUS AP250D weight. The powder samples were heated from room temperature to 323 K with a heating rate of 10 K/min. Then the samples were dried at 323 K for 2 hours, followed by 2 h at 373 K, 6 h at 423 K, 2 h at 373 K and lastly 2 more hours at 323 K. The heating rate between all the steps were 10 K/min. The weight loss in percentage was calculated from the maximum recorded weight of the sample before the first heating step in

order to make the samples comparable for further study.

The second drying process were conducted for all the samples. The process was intended to quantify the amount of water in the samples and to better understand the temperature range of the dehydroxylation of the different samples. The samples were put in an atmosphere with 43% RH for at least 24 hours. The heating process started from 298 K and the samples were heated to 573 K with a heating rate of 5 K/min. The heating was done with a N_2-gas flow.

To quantify the amount and duration of hydration during the second drying process for Fe(II)-FHT-sim, Fe(II)-FHT-pre, Fe(III)-FHT-sim, and Fe(III)-FHT-pre, the samples were measured at 298 K for 13 hours.

4 Result

4.1 XRD

4.1.1 European Synchrotron Radiation Facility

Sample Zn-FHT, Mg-FHT, Cu-FHT, Ni-FHT and Mn-FHT were all attempted dried, but immediately hydrated when cooled. Therefore, these samples were not pressurized with CO_2. Figure 10 for Cu-FHT shows an example that the criteria for a dry clay was not fulfilled. As the temperature dropped, the q-vector decreased drastically. The d-spacing goes from 10.45 Å to 11.63 Å and thus water migrated back into the interlayer.
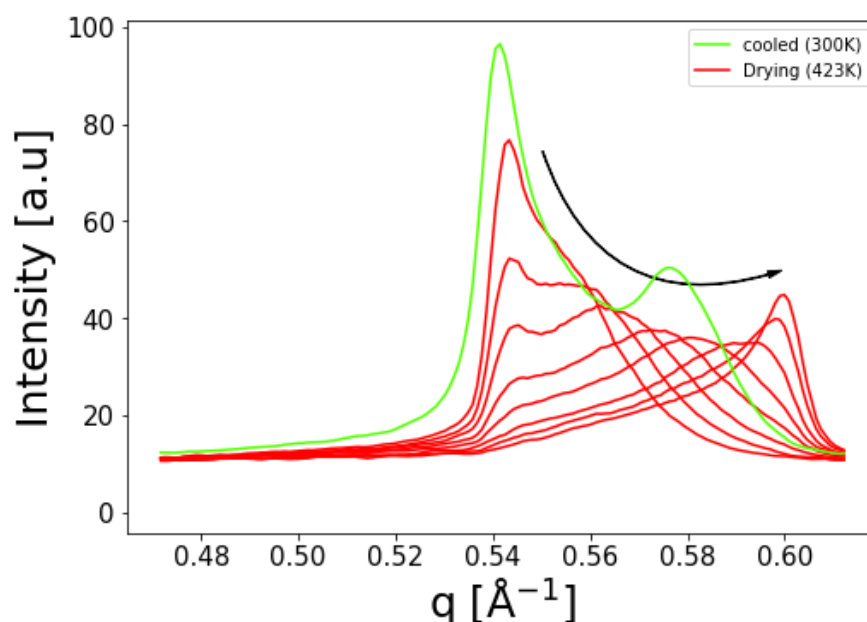

Figure 10: XRD measurement of 001 bragg peak for the Cu-FHT. The drying process was at 423 K (red plots) starting from q=0.54 Å^{-1} to q=0.60 Å^{-1}, where the arrow indicate the general movement of the peak while drying. The temperature is at 300 K for the cooled peak (green plot).

This was not the case for Fe(III)-FHT and the cooling which is depicted in Figure 11. During drying the 001 bragg peak went from d-spacing of 13.69 Å at 300 K (leftmost red peak at q= 0.459Å^{-1}) to a d-spacing of 10.80 Å at 423 K (rightmost red peak). The bragg peak remained stationary during cooling, where the temperature was brought down again to 300 K (green).
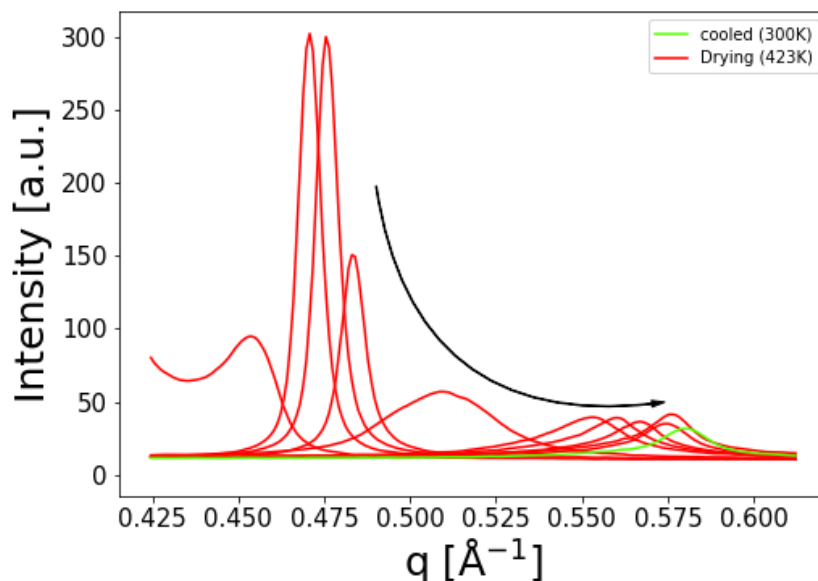
Figure 11: XRD measurement of 001 bragg peak for Fe(III)-FHT. The temperature goes from 300 K to 423 K and shows the drying process of FeFHT from q=0.459 Å^{-1} to q=0.582 Å^{-1} (red). The arrow indicate the general movement of the peak while drying. The cooled sample is measured at 300 K (green).

The Fe(III)-FHT was then put under stepwise pressures at 300 K of 18, 30, 42, 50, 2 and 0 bar. As Figure 12 shows the 001 bragg peak swells from dried state at 10.74 Å (q=0.585 Å^{-1}) and to 11.12 Å (q=0.56 Å^{-1}) for 18 bar with minor increases for each of the consecutive pressure steps at 30, 42 and 50 bar.

The intensity of the peak increased with higher CO_2 pressure and could be seen if the offset is removed. The relative change in d-spacing is 0.47 Å from dried Fe(III)-FHT to 50 bar pressure. Figure 12 also contains 2 bar and 0 bar at 300 K after high pressure CO_2. The peak at 2 and 0 bar stayed at 11.21 Å (q=0.560 Å^{-1}).

Lastly, the Fe(III)-FHT powder was heated to 423 K at 0 bar and the d-spacing went back to 10.76 Å (q=0.584 Å^{-1}). This is highly comparable to the d-spacing of the dried Fe(III)-FHT. The heating process after CO_2 exposure gave a decrease in swelling starting at 326 K. The heating continued for 20 minutes and the temperature rose linearly from 300 to 423 K. Figure 13 shows the increase in scattering vector, q, as a function of temperature.
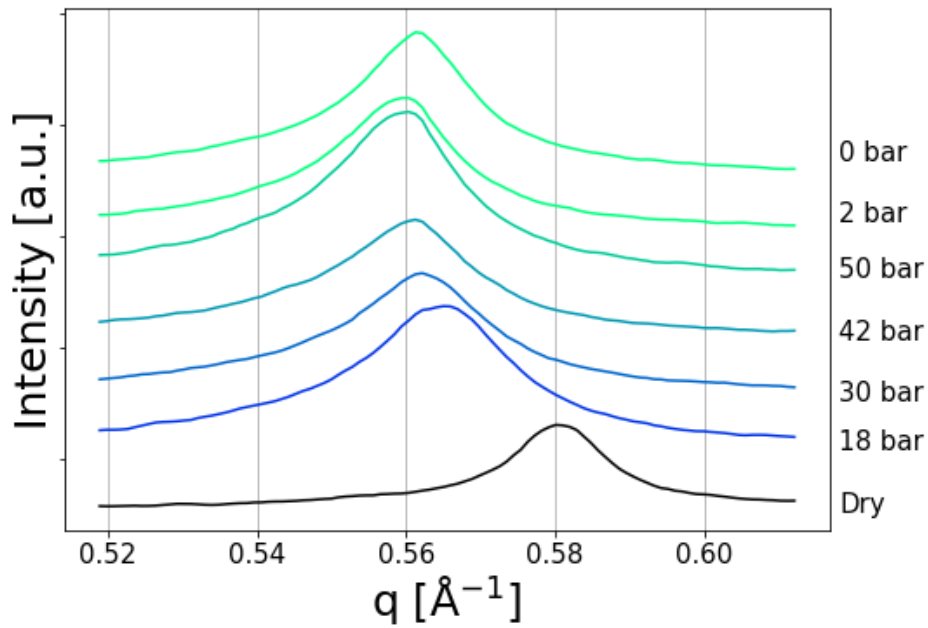
Figure 12: XRD measurement of Fe(III)-FHT sample under CO_2 pressure. The order of the steps are 18, 30, 42, 50, 2 and 0 bar all at 300 K. The curves have been shifted by an offset for clarity.
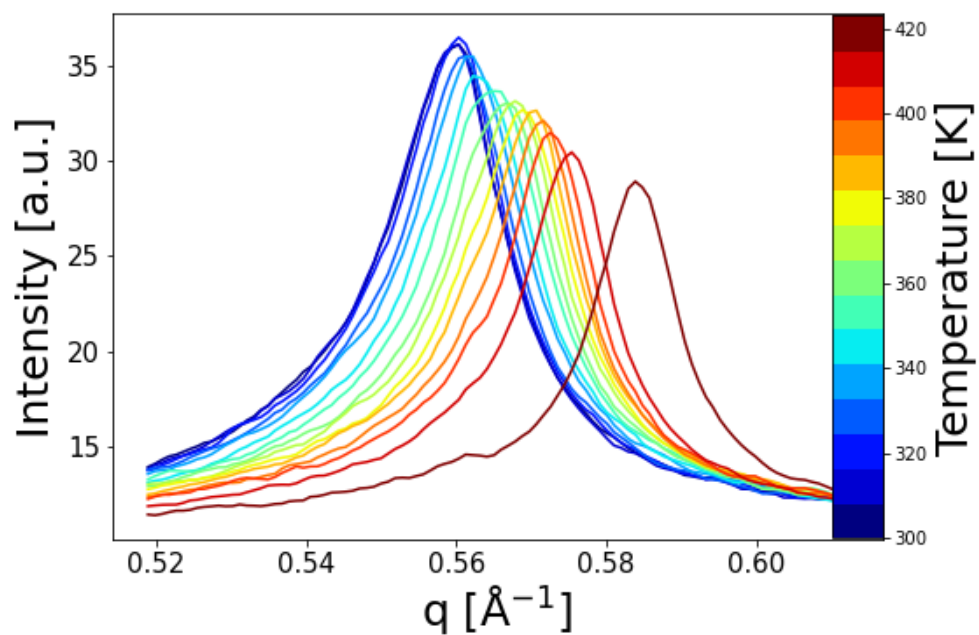

Figure 13: CO_2 release upon heating from 300 K to 423 K.

Table 5 shows the time, temperature and d-spacing for each pressure steps.

Table 5: Pressure, time, temperature and d-spacing at each step of the Fe(III)-FHT sample. The steps are in chronological order. The hyphen is put between the start value and end value of the given parameter.

Pressure (Bar)	Time (min)	Temperature (K)	d-spacing (Å)
0 (Drying)	47	423	13.69-10.80
0 (Cooling)	8	423-300	10.74
18	12	300	11.12
30	10	300	11.18
42	17	300	11.20
50	53	300	11.22
2	9	300	11.22
0	15	300	11.20
0 (Heating)	20	300-423	11.20-10.93
0	30	423	10.93-10.76

The basal spacing for all the steps are shown in Figure 14 and show a clear hysteresis behavior.
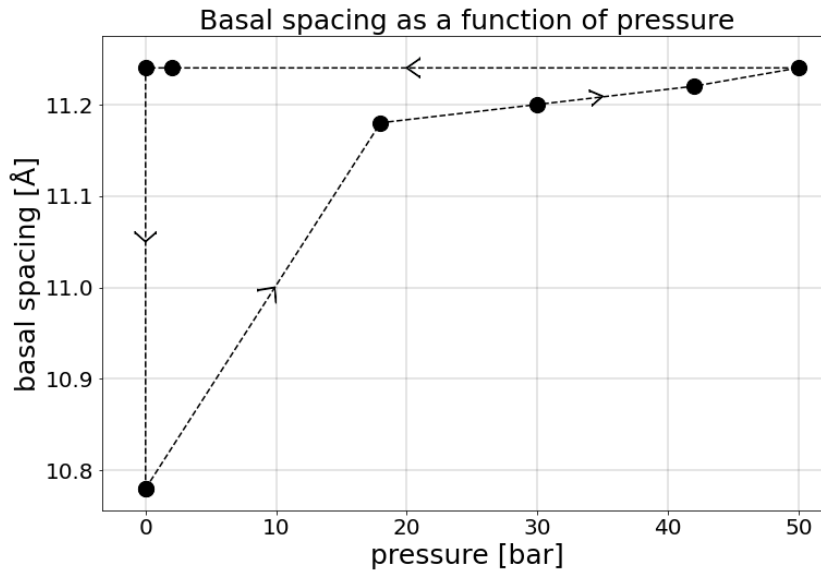

Figure 14: The basal spacing of Fe(III)-FHT sample under CO_2 pressure. 0, 18, 30, 42, 50, 2 and 0 bar at 300 K and heated to 340 K at 0 bar. The arrows indicate the order of the different steps, starting from the bottom left corner.

Figure 15 depicts the 2 dimensional diffractogram of Fe(III)-FHT and the corresponding azimuthally integrated plot. The 001, 002 and 003 bragg peaks are shown for clarification.
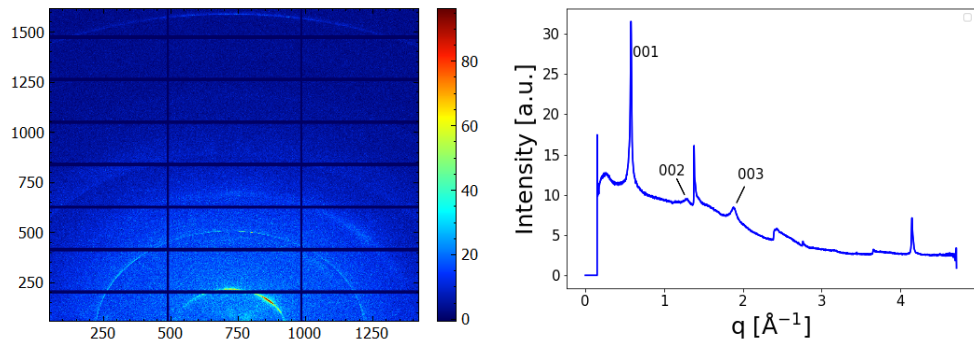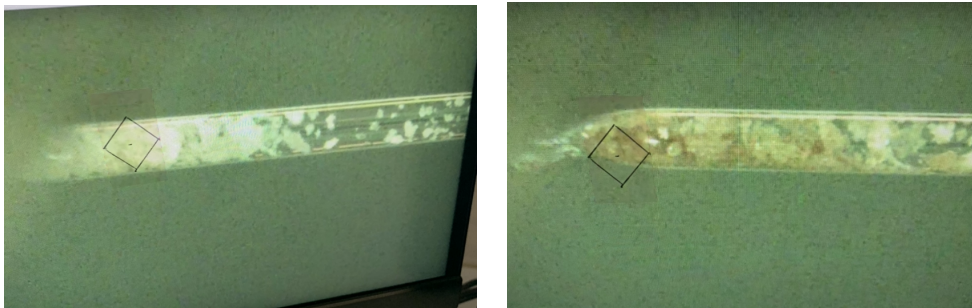

(a) Diffractogram of Fe(III)-FHT as measured at the beamline.

(b) Azimuthally integrated diffractogram of Fe(III)-FHT (I vs q). The 001, 002 and 003 bragg peaks are marked in the figure

Figure 15: Data from ESRF for Fe(III)-FHT

Figure 16 shows a change in color of the Fe(III)-FHT powder from white (before measurement) to brown (after measurement). Both pictures show that the Fe(III)-FHT clay powder is spread out.

(a) Fe(III)-FHT before measurement.

(b) Fe(III)-FHT after measurement

Figure 16: The change in color of Fe(III)-FHT from measurement.

Figure 17 depicts the azimuthally integrated plot of wet Fe(III)-FHT-sim. The higher order bragg peaks are highly visible (001, 002 and 003 peaks marked).
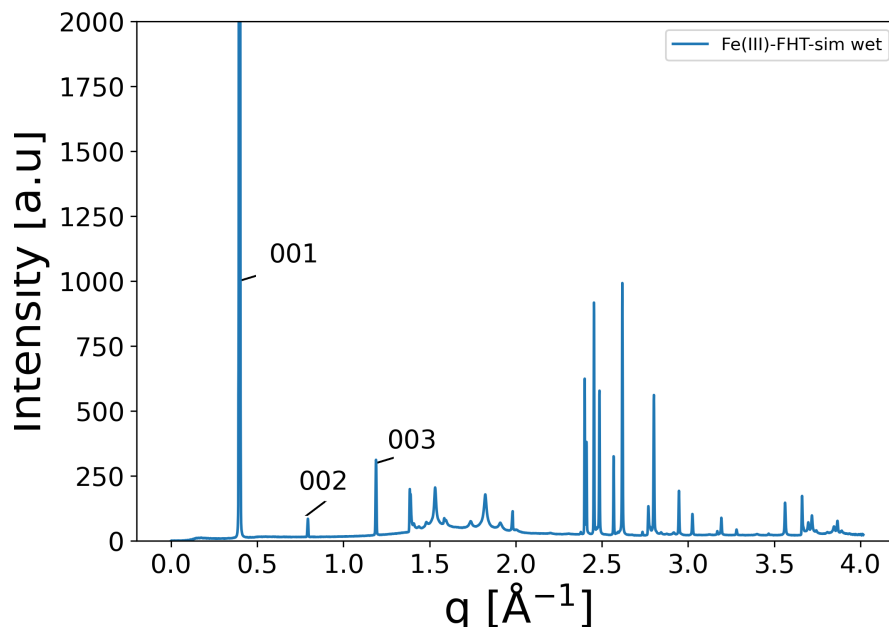

Figure 17: Azimuthally intergrated diffractogram of Fe(III)-FHT-sim (I vs q). The 001, 002 and 003 bragg peaks are marked in the figure.

Figure 18 shows the difference in peak position of the 001 bragg peak for the Fe(III)-FHT-sim sample. The peak positions for the different samples are as follows: the wet sample measures 15.84 Å, the dry sample measures 10.57 Å, the cooled sample measures 10.56 Å, and after 3 hours at 40 bar CO_2, it reaches 11.11 Å. The 40 bar CO_2 001 peak is a double peak.
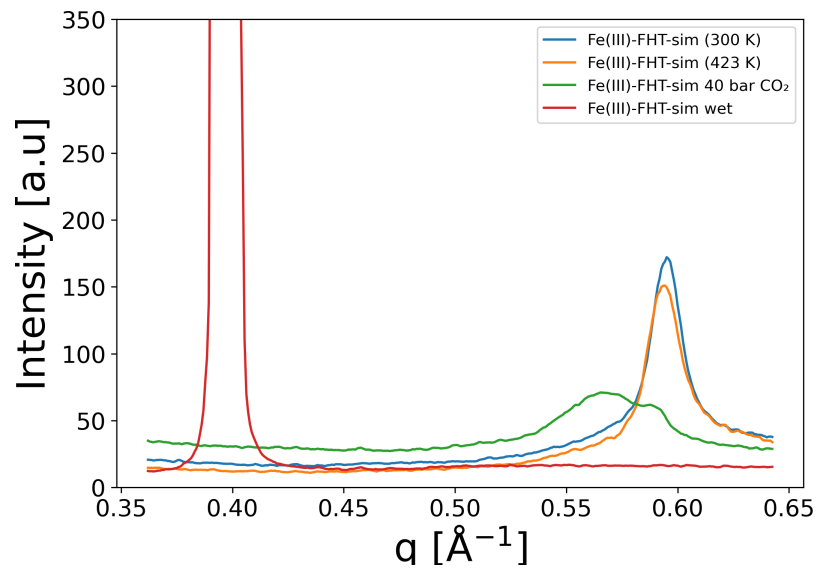

Figure 18: Azimuthally integrated diffractogram of wet dry, cooled and pressurized Fe(III)-FHT-sim (I vs q).

Figure 19 shows the development for the 001 peak of the CO_2 pressurized sample. The high q top of the double peak stays at the same position as for the dried 001 peak. The low q top emerges and shifts to lower q during the CO_2 exposure. The d-spacing of the top with the highest intensity is plotted in Figure 20. After approximately 40 minutes the intensity of the low q top is greater than for the high q top. The d-spacing for the low q peak also exhibits a swelling throughout the 3 hours of exposure to 40 bar CO_2 and goes from 10.9 Å to 11.11 Å.
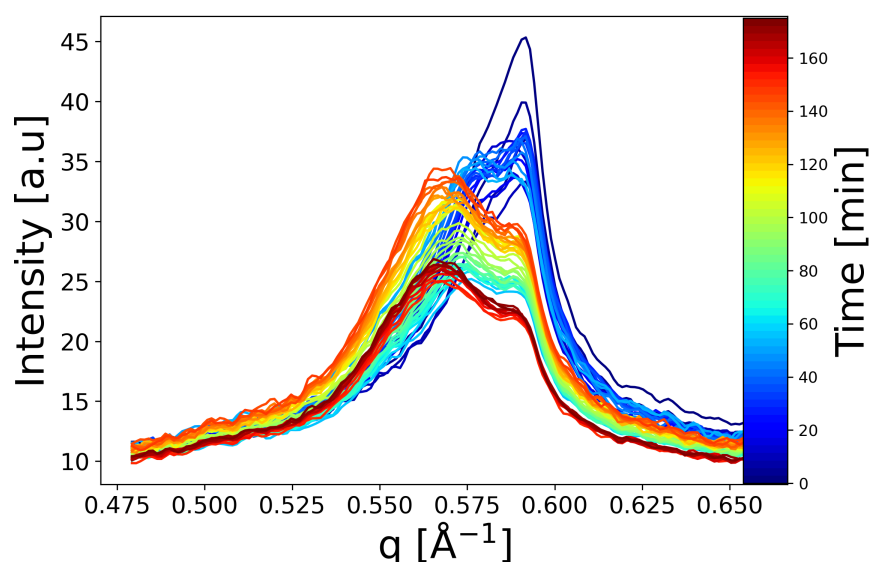

Figure 19: The change of the 001 peak for Fe(III)-FHT-sim during 3 hours exposure at 40 bar CO_2 (I vs q).
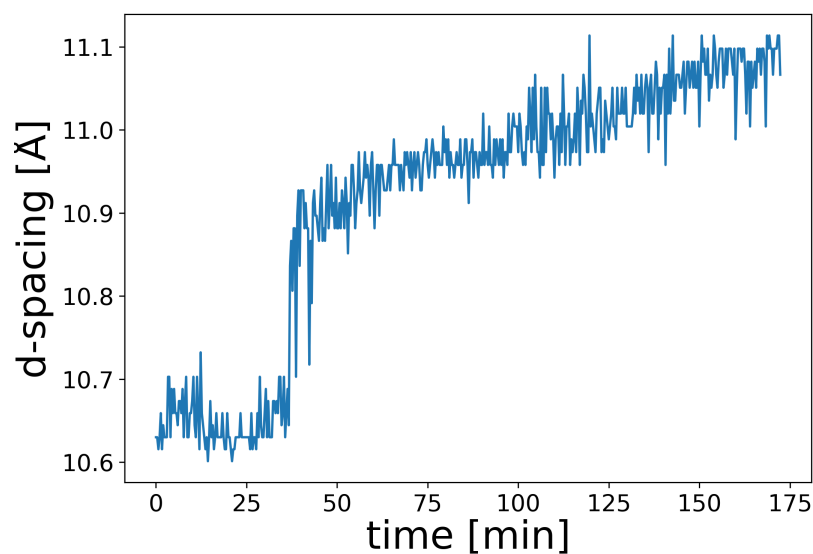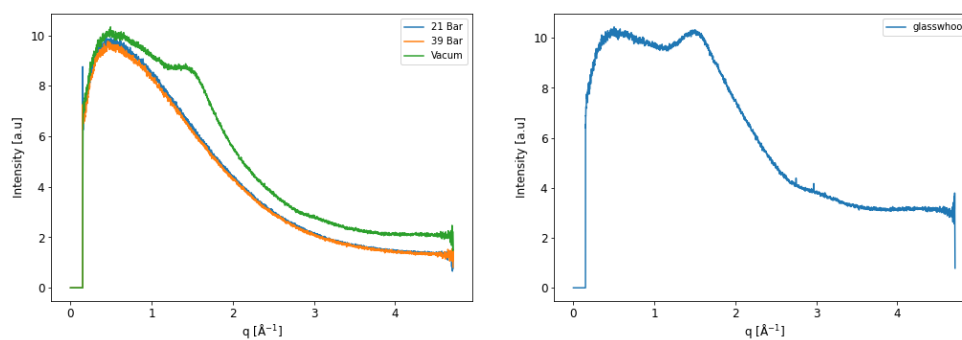
Figure 20: The d-spacing change for highest intensity top for the 001 peak for Fe(III)-FHT-sim, during 3 hours exposure of 40 bar CO_2 (d-spacing vs time).

Figure 21 shows the measurement for empty capillary at vacuum, 21 bar of CO_2, 39 bar of CO_2 and glasswool.

(a) Diffractogram of empty capillary with vacuum and 21 and 39 bar of CO_2.

(b) Diffractogram of capillary filled with glasswool.

Figure 21: Background results of the different components from the setup

4.1.2 D8 Focus

Figure 22 shows the dried and wet Fe(III)-FHT and the background from the empty domeholder. The results were converted from 2θ to d-spacing. There are 4 peaks from the empty domeholder at approximatly 4.5 Å, 10.5 Å, 16.5 Å and 27 Å. Additionally, there is a linear increase in intensity for the background between 15-30 Å. Both the dry and wet Fe(III)-FHT have peaks at the same d-spacing as the empty domeholder.
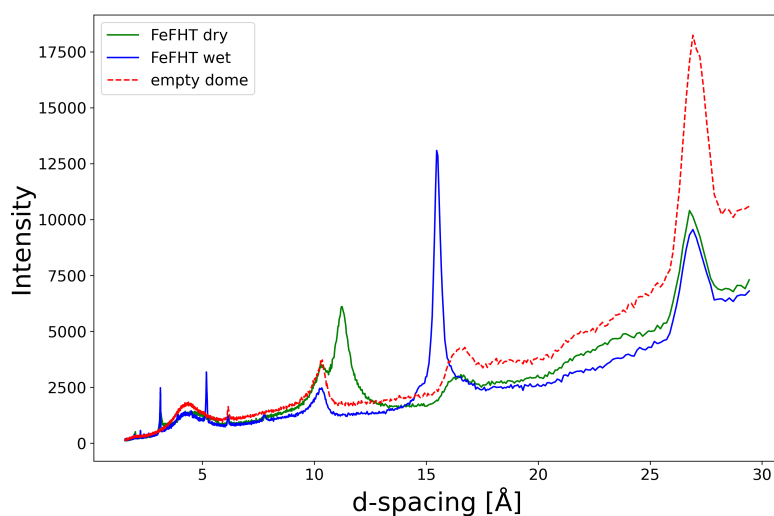

Figure 22: The D8 focus XRD measurement of the Fe(III)-FHT sample, dried powder (green), wet powder (blue) and background measurement (red, dashed).

Figure 23 shows only the 001 bragg peaks (d-spacing from 8.5-18 Å) of the dry and wet Fe(III)-FHT and the background from the sample holder. The d-spacing for the wet and dry sample is 15.47 Å and 11.24 Å, respectively. There is a shoulder at the left side of both 001 peaks and the shoulder for the dried sample is relatively larger than the wet shoulder when compared to the height of the 001 peaks. The intensities of the wet and dry samples are equal at the position of the background peak at 16.5 Å, but have an intensity difference at the background peak located at 10.5 Å.

The following XRD measurements for Fe(III & II)-FHT-sim & -pre were performed with the dried samples in a dome holder and the wet samples without. The measurements were converted from 2θ to d-spacing. The four peaks from the empty dome holder and the linear increase in intensity between 15-30 Å were also observed, as described for the Fe(III)-FHT.
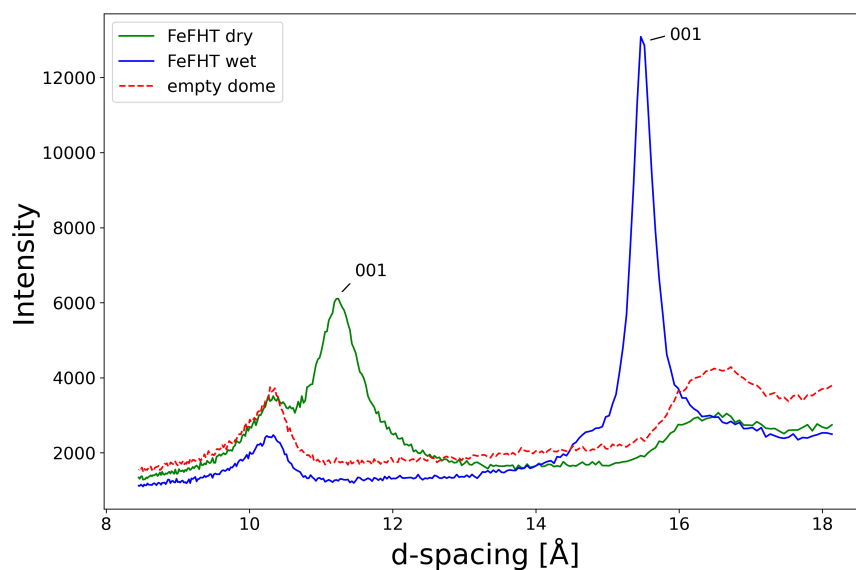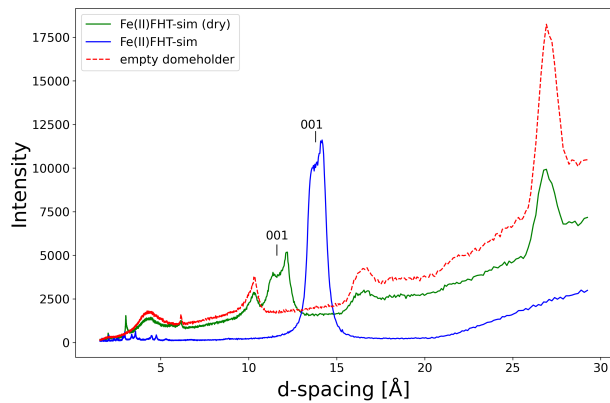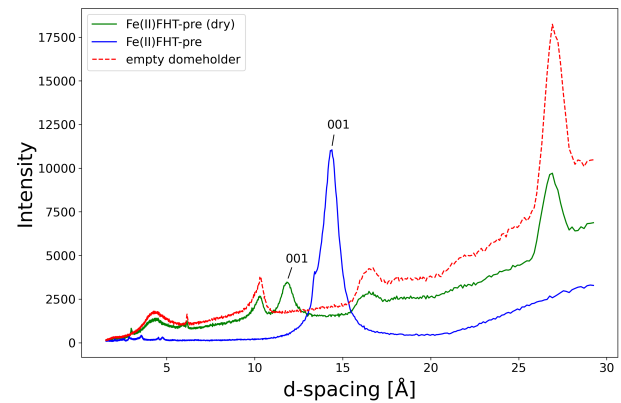
Figure 23: The 001 bragg peak XRD of the Fe(III)-FHT sample, dried powder (green), wet powder (blue) and background measurement (red, dashed).

Figure 24a shows the XRD of Fe(II)-FHT-sim, where the wet sample exhibits lower d-spacing peaks (below 5 Å) that are more visible when compared to the XRD of Fe(II)-FHT-pre from Figure 24b. Figure 24c displays the 001 bragg peaks for Fe(II)-FHT-sim. Each 001 peak exhibits a higher-intensity top (on the right side of the 001 peak) with a smaller top (on the left side of the 001 peak) with a d-spacing of 14.14 Å and 13.59 Å for wet sample and 12.12 Å and 11.32 Å for dry sample. Fe(II)-FHT-pre 001 bragg peak have a d-spacing of 14.38 Å (wet) and 11.83 Å for dry sample, as Figure 24d shows.

(a) Fe(II)-FHT-sim.

(b) Fe(II)-FHT-pre.
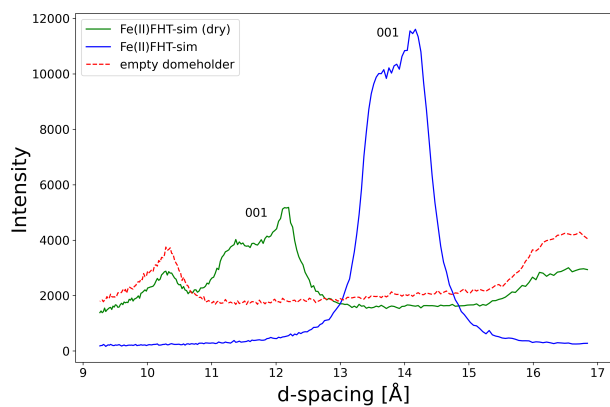
(c) Fe(II)-FHT-sim 001 peak.

(d) Fe(II)-FHT-pre 001 peak.

Figure 24: The D8 focus XRD measurement of the Fe(II)-FHT-sim & -pre sample, dried powder (green), wet powder (blue) and background measurement for dry sample (red, dashed).

The XRD measurement of Fe(III)-FHT-sim, Figure 25a, and Fe(III)-FHT-pre, Figure 25b, also shows that the -sim sample have higher intensity peaks for d-spacing below 5 Å, when compared to the -pre sample. Figure 25c displays the 001 bragg peak of Fe(III)-FHT-sim which have a d-spacing of 13.26 Å (wet) and 11.60 Å (dry). The 001 bragg peak for Fe(III)-FHT-pre from Figure 25d shows a d-spacing of 13.33 Å (wet) and 11.80 Å (dry)
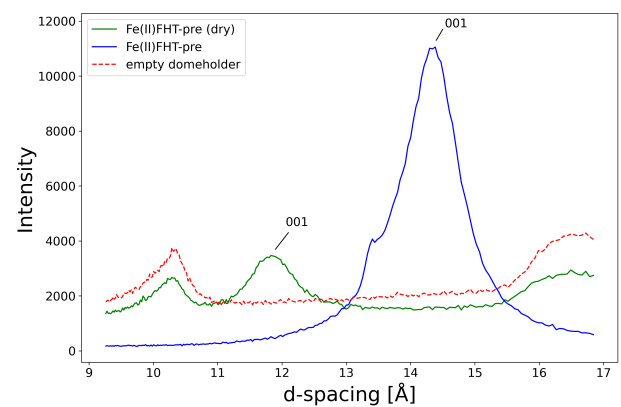
(a) Fe(III)-FHT-sim.
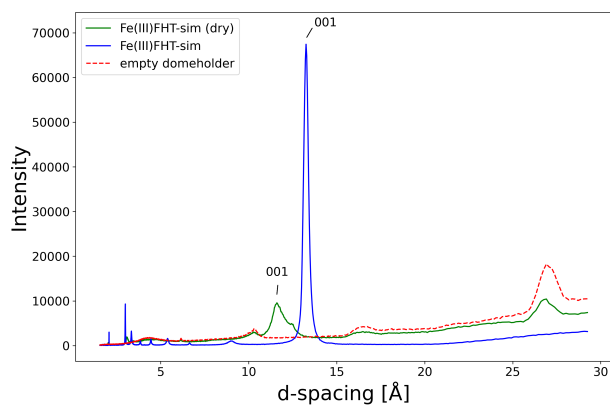
(b) Fe(III)-FHT-pre.
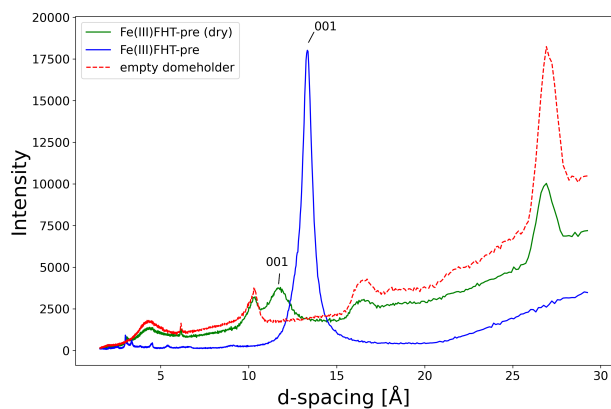
(c) Fe(III)-FHT-sim 001 peak.

(d) Fe(III)-FHT-pre 001 peak.

Figure 25: The D8 focus XRD measurement of the Fe(II)-FHT-sim & -pre sample, dried powder (green), wet powder (blue) and background measurement for dry sample(red, dashed).
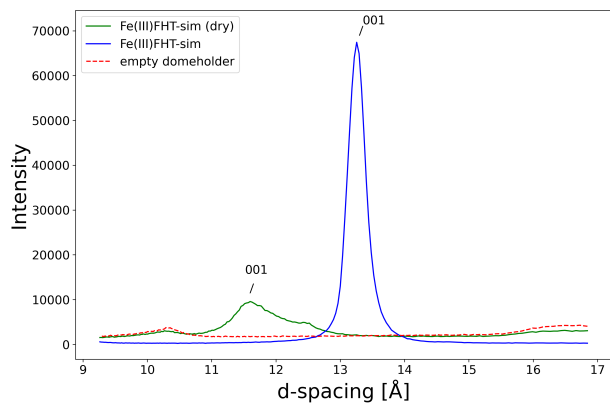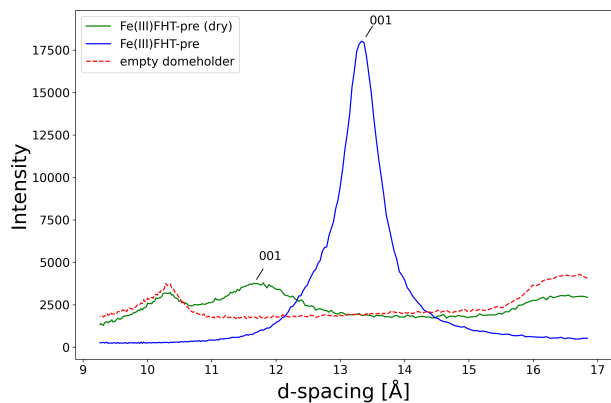
4.2 TGA

The first drying process from Figure 26 shows that all clay samples had a weight reduction at 323 K and all except Ni-FHT had another clear weight reduction at 373 K. Only Cu-FHT had a third clear weight reduction from 373K to 423 K. All sample had a minor weight loss at 423 K and every sample except Cu-FHT had a continuous mass loss during the 6 h at 423 K. Another distinction visible at 423 K was that Cu-FHT, Mg-FHT and Ni-FHT had a maximum mass loss of 8.5-10% and Mn-FHT, Zn-FHT and Fe(III)-FHT had a maximum mass loss of 14.5-17% . The cooling process showed that only Cu-FHT, Zn-FHT and Mn-FHT gave a clear weight increase. The weight increase were 4.5% for Cu-FHT, 3.7% for Zn-FHT and 2.6% for Mn-FHT. Mg-FHT had a small weight increase (<0.5%) during cooling. Fe(III)-FHT had a small continuous weight reduction from 373 K and all the way to the end of the measurement. This was the only sample with a weight reduction upon cooling. Ni-FHT showed no detectable weight change upon cooling.

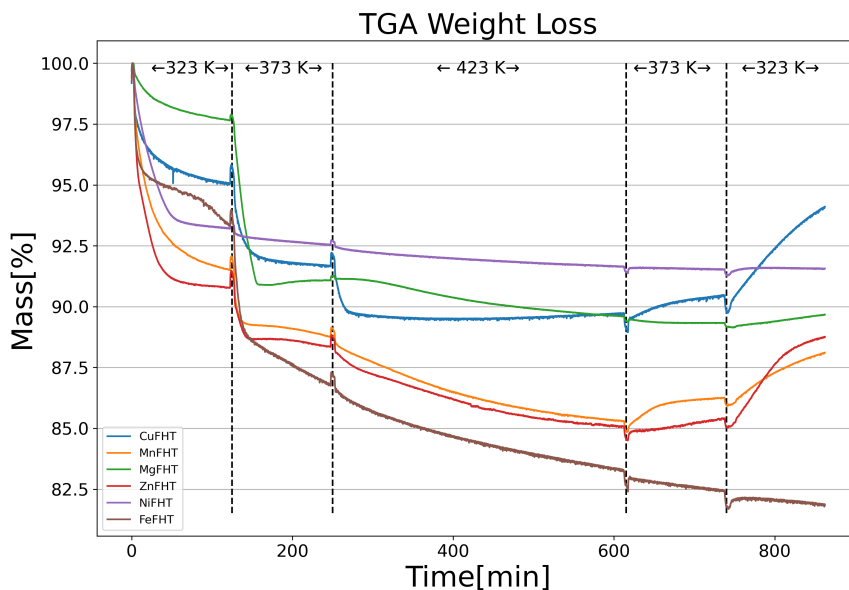**Figure 26:** The weight loss in percentage of Cu-FHT, Mg-FHT, Mn-FHT, Zn-FHT, Ni-FHT and Fe(III)-FHT as a function of time. The different temperature regimes are separated with vertical dotted lines.

The heating gave a darker color for all clay samples, as shown in Figure 27. The leftmost part of each sample were the samples put in 43% relative humidity for >24h, the middle were shortly heated to 573 K and the right-

most part were hydrated with water and dried at 298 K. All samples except Ni-FHT gave a lighter color after mixed with water, but did not return to the original color.
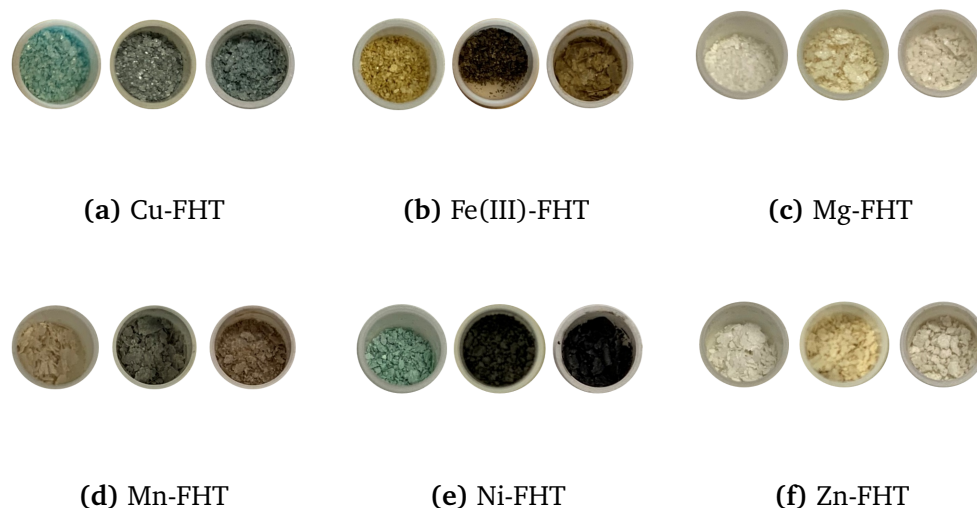

(a) Cu-FHT **(b)** Fe(III)-FHT **(c)** Mg-FHT

(d) Mn-FHT **(e)** Ni-FHT **(f)** Zn-FHT

Figure 27: Clay samples before (left) and after (middle) TGA measurement of temperatures up to 573 K. The samples were then mixed with water and dried at 298 K (right).

Figure 28 shows the second heating process of 573 K for Cu-FHT, Ni-FHT and Zn-FHT with T_d marked on the measurements as a vertical dashed line (see Table 4). Figure 29 shows the TGA measurement of the second heating process for Mn-FHT, Fe(III)-FHT and Mg-FHT, which have T_d either unknown or outside the temperature regime of the heating process. The red dashed lines are the DTG curve (derivatives) of the mass loss for each sample. The derivatives have been smoothed out over several measurements in order to prevent local fluctuations to misrepresent the general mass loss trend.

Cu-FHT: The first mass loss regime is clearly visible as a valley in the derivative (DTG curve) and gave a mass loss of 6.7% from 298 K and to the T_d (423 K), seen in Figure 28a. Approximately at T_d there is a peak in the mass loss rate which separate the two different mass loss regimes. The first valley is wide and consist of two separate minimums. The second valley, after the T_d peak, has only one minimum and here Cu-FHT lost 3.2% mass from T_d up to 460 K and then showed no mass loss.

Ni-FHT: As shown in Figure 28b, Ni-FHT had similar behavior as Cu-FHT except that there was a temperature gap between the first and second weight loss. Both samples had the second mass loss regime starting just
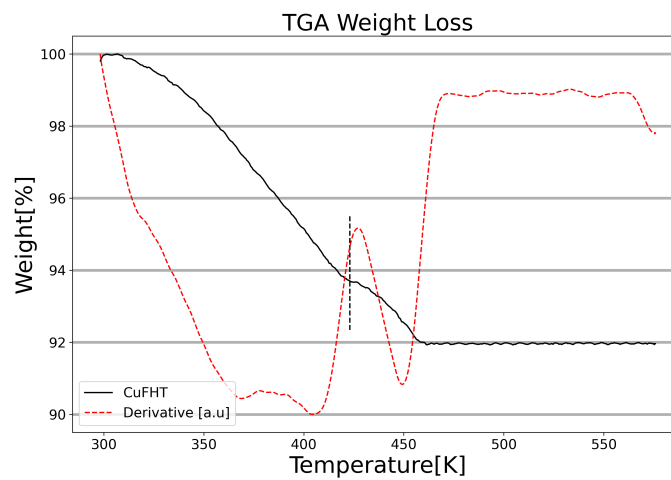
(a) Cu-FHT.
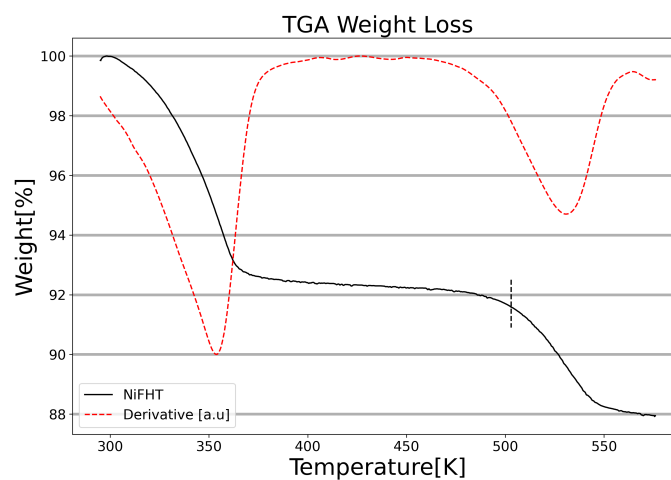
(b) Ni-FHT.
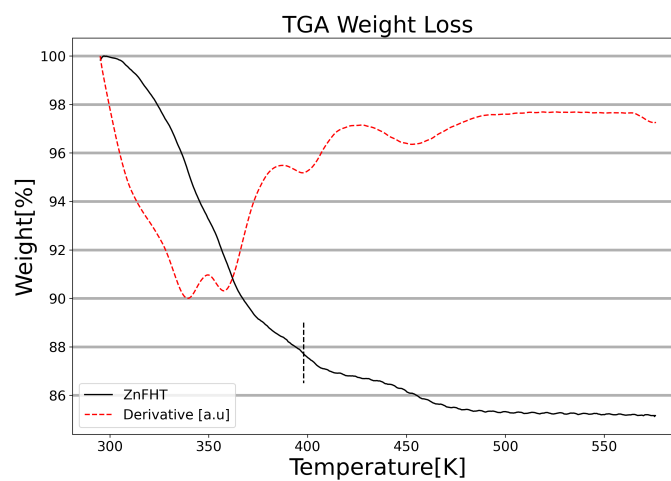
(c) Zn-FHT.

Figure 28: Cu-FHT, Ni-FHT and Zn-FHT heated from 298 K to 573 K with a heating rate of 5 K/min. The T_d within this temperature range are plotted as a black vertical dotted line for the respective samples. The red dotted line is the derivative with arbitrary units for better comparisons.

after T_d was reached. The first and second mass loss happened at 298-375 K and 473-573 K and had a mass loss of 7.7 % and 4.3%, respectively. Both mass losses gave a DTG curve with only one minimum each.

Zn-FHT: There were less distinct rates of mass loss, as seen in Figure 28c. The T_d temperature for Zinc hydroxide does not lie between two separate valleys of the derivative, as for both Cu-FHT and Ni-FHT. The derivative shows there is one valley with two different minima before T_d, which account for most of the mass loss. The remaining mass loss after T_d is separated into two minor minima. The mass loss stopped at 473 K and gave a total mass loss of 14.8%. From the derivative one can divide the mass loss rates into 4 different regimes, each separated by the small peaks.

Mn-FHT: Figure 29a shows a clear distinction in mass loss rates separated at approximately 425 K. The mass loss from 300-425 K was 12.4% and the second mass loss step from 425K to 480 K was 1.9%, from there on the mass remained constant up to 573 K.

Fe(III)-FHT: Figure 29b shows two different mass loss steps, separated at 360 K. The first from 300 K to 360 K had a mass loss of 9.4%. The second mass loss step from 360-550 K was at 4.6% if one include the small mass loss from about 400-550K.

Mg-FHT: Figure 29c shows that Mg-FHT had two different mass loss regimes before 410 K, separated with a rate change at 355 K (peak at DTG curve). The mass loss from 300-355 K was 5% and the mass loss from 355-410 K was 6.4%. There was a third mass loss step at 450-490 K with a mass loss of 1.9% before the mass became constant.
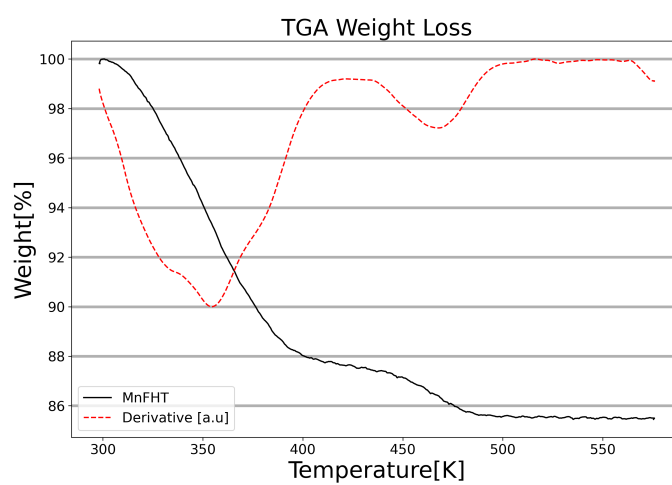
(a) Mn-FHT.
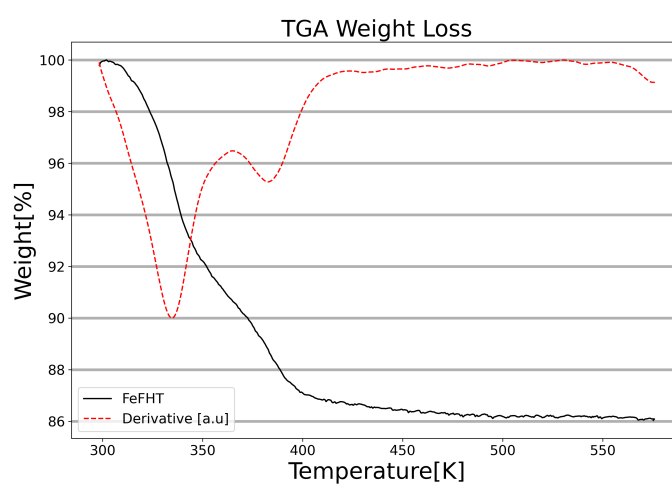
(b) Fe(III)-FHT.
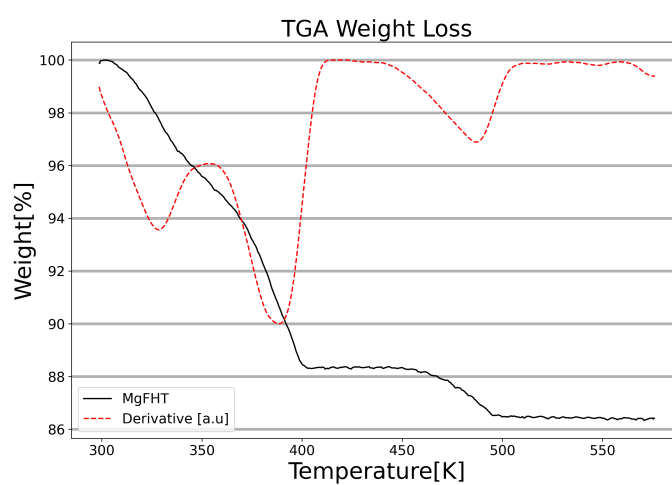
(c) Mg-FHT.

Figure 29: Mn-FHT, Fe(III)-FHT and Mg-FHT heated from 298 K to 573 K with a heating rate of 5 K/min. The red dotted line is the derivative with arbitrary units for better comparisons.

The other Fe-FHT samples exhibited similar weight loss behavior as the first Fe(III)-FHT shown in Figure 29b, characterized by a large mass loss valley in the derivative with a minimum below 350 K. This minimum is followed by another mass loss region, indicated by a widening of the valley. Furthermore, all subsequent Fe-FHT samples exhibited a minor, continuous mass loss between 450 K and 573 K.

Fe(II)-FHT-sim: Figure 30a shows a weight loss of 13.2% between 298-410 K and a mass loss of 1.4% after 410 K with another minimum at 475 K.

Fe(II)-FHT-pre: Figure 30b shows a weight loss of 14.0% between 298-425 K and a mass loss of 2.2% after 425 K with another minimum at 475 K.
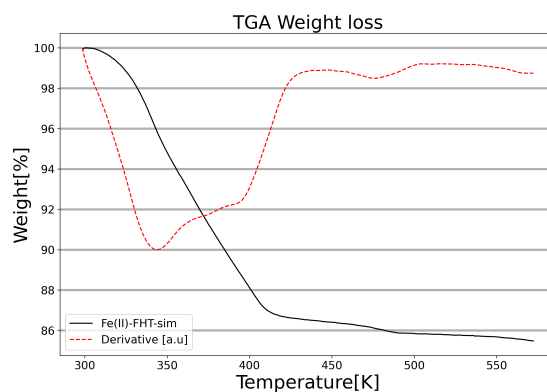
(a) Fe(II)-FHT-sim.
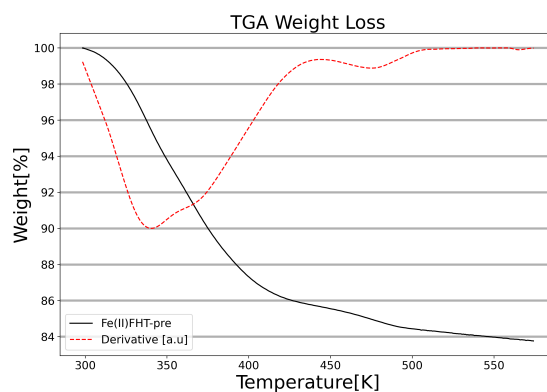
(b) Fe(II)-FHT-pre.

Figure 30: Fe(II)-FHT and Fe(II)-FHT-pre heated from 298 K to 573 K with a heating rate of 5 K/min. The red dotted line is the derivative with arbitrary units for better comparisons.

Fe(III)-FHT-sim: Figure 31a shows a weight loss of 14.3% between 298-415 K and a mass loss of 1.2% after 415 K.

Fe(III)-FHT-pre: Figure 31b shows a weight loss of 13.7% between 298-430 K and a mass loss of 1.6% after 430 K.
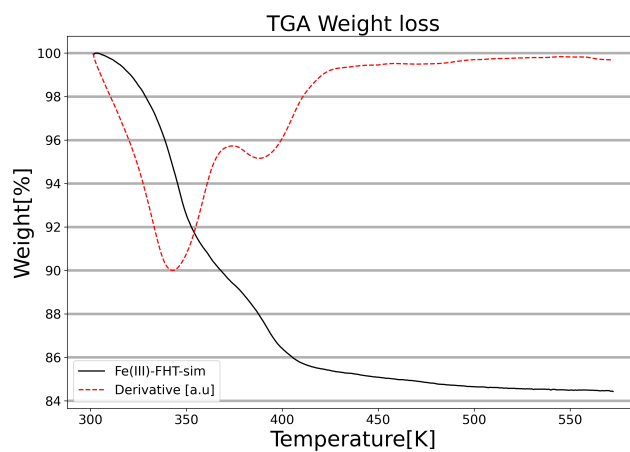
(a) Fe(III)-FHT-sim.
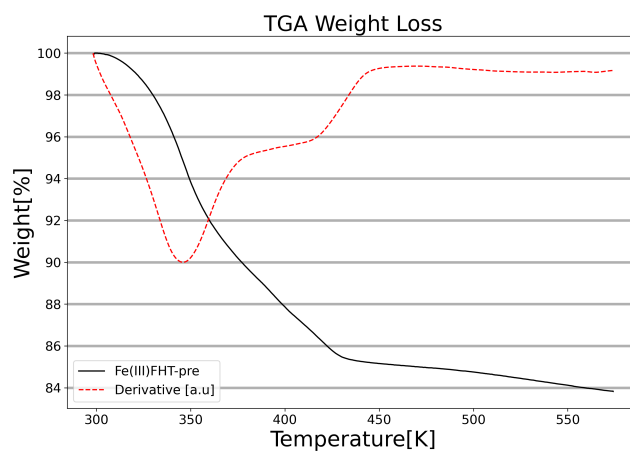
(b) Fe(III)-FHT-pre.

Figure 31: Fe(III)-FHT-sim and Fe(III)-FHT-pre heated from 298 K to 573 K with a heating rate of 5 K/min. The red dotted line is the derivative with arbitrary units for better comparisons.

Only Fe(II)-FHT-pre and Fe(III)-FHT-pre shows a clear weight gain at 298 K after drying, as can be seen in Figure 32. Fe(II)-FHT-pre had a maximum weight gain of 2.42% after 4 h. Fe(III)-FHT-pre had a weight gain of 1.68% after 13 hours. Both Fe(II)-FHT-sim and Fe(III)-FHT-sim had a weight increase below 0.25%.
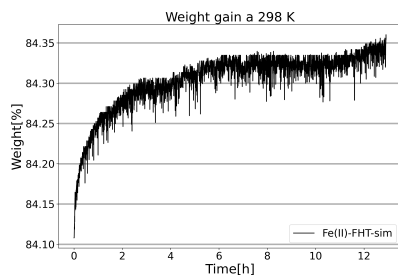
(a) Fe(II)-FHT-sim.
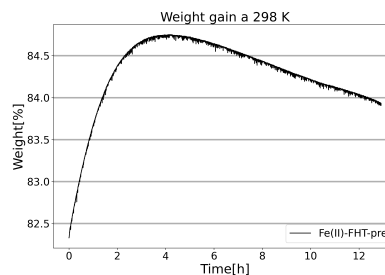
(b) Fe(II)-FHT-pre.
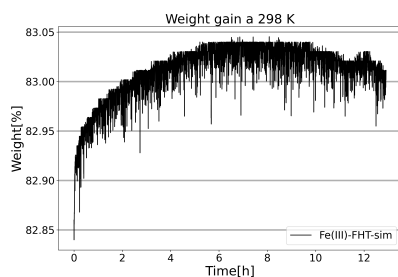
(c) Fe(III)-FHT-sim.
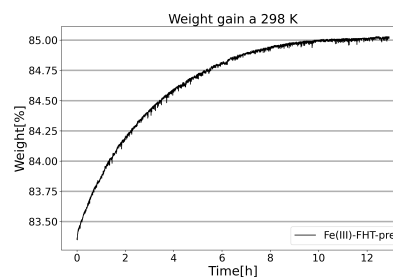
(d) Fe(III)-FHT-pre.

Figure 32: Weight gain for Fe(II)-FHT-sim, Fe(II)-FHT-pre, Fe(III)-FHT-sim and Fe(III)-FHT-pre at 298 K after drying.

Figure 33 shows the thermal expansion of the TGA weight balance. An empty crucible were heated and cooled twice at 10 K/min and gives weight change of less than 1%.
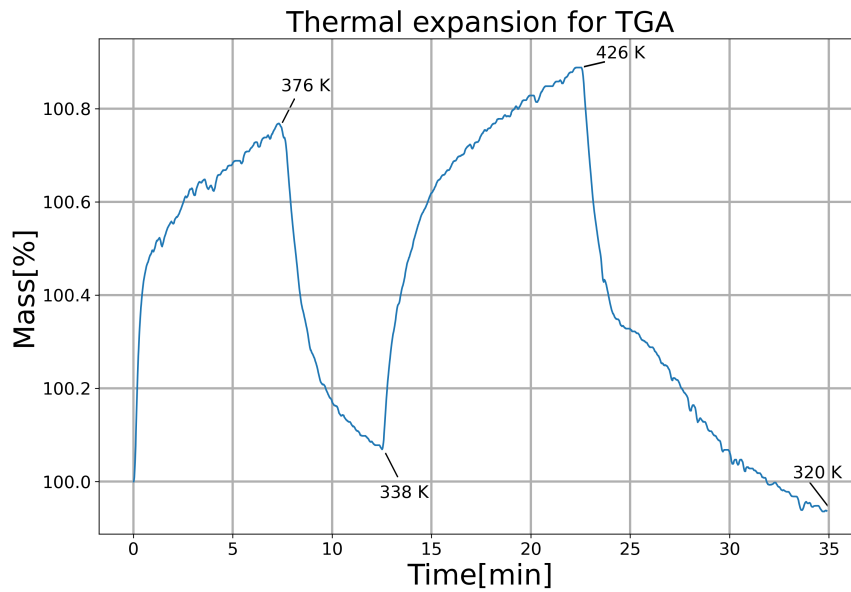
Figure 33: An empty crucible was heated and cooled twice between 338-426 K to show the weight change due too thermal expansion of the TGA.

Table 6 shows the results for each sample for the TGA.

Table 6: TGA results for each sample. M_i is the starting weight of each sample after hydration at 43% relative humidity, T_{DTG} is the temperature of the global minimum of the DTG curve for each sample and T_{max} is the temperature at which the weight loss stops.

Sample	M_i (mg)	T_{DTG} (K)	Total mass loss (%)	T_{max} (K)
Cu-FHT	10.81	404	9.9	460
Ni-FHT	6.08	354	12	573
Zn-FHT	9.18	339	14.8	473
Mn-FHT	6.62	354	14.3	480
Fe(III)-FHT	11.21	334	14	550
Mg-FHT	8.84	388	13.3	490
Fe(II)-FHT-sim	14.11	344	14.6	>573
Fe(II)-FHT-pre	11.31	340	16.2	>573
Fe(III)-FHT-sim	10.49	343	15.5	>573
Fe(III)-FHT-pre	13.09	345	15.3	>573

5 Discussion

5.1 XRD

5.1.1 Fe(III)-FHT

In this study the d-spacing was found to be the same for dried Fe(III)-FHT and heated Fe(III)-FHT after CO_2 exposure, suggesting that the clay goes back to the initial state and the intercalation is therefore reversible at 423 K. This was also what Michels et al. found for the Li-FHT which showed retention of CO_2 up to 308 K [13]. Loganathan et al. showed that Cs-Hectorite had desorption of CO_2 at 323 K combined with vacuum [38]. The observed hysteresis behavior from Figure 14 has been reported repeatedly for hectorites and montmorillonites [2, 5, 13, 15, 38, 39].

The 001-peaks of the CO_2 exposed Fe(III)-FHT gave a symmetric peak structure. Normally, a weight towards higher q-values indicate not fully intercalation of the CO_2 molecules in all interlayers [2].

As a pressure of CO_2 was put on Fe(III)-FHT the swelling shown in Figure 12 was caused by CO_2 entering the interlayer. The swelling was 0.47 Å and the kinetic diameter of CO_2 (3.3 Å) is much larger. This small swelling compared to the kinetic diameter suggest that the synthesis of Fe(III)-FHT clay did not give complete order interstratification, despite the fact that there is no weight towards higher q. In comparison, the swelling of Li-FHT was 2 Å (from 10.2 to 12.2 Å) with pressurized CO_2 of 50 bar at 253 K (liquid CO_2) [2].

The d-spacing increased for higher pressures. This suggest that the amount of CO_2 increases when the pressure becomes higher. The intensity increased as the pressure of CO_2 increased, which is the opposite of what was expected. As Figure 21a shows, the intensity would decrease for higher CO_2 pressure, because more CO_2 in the atmosphere inside and around the powder would absorb more X-rays. A possible explanation is that the structure becomes more ordered as more CO_2 enters the interlayer, which will give more similar scattering vectors and an increase in intensity of the peak. One should also remember that for powder X-ray diffraction, the intensity of different measurements is usually not comparable. This is because the grainsize and orientation can vary for different parts of the powder. The diffractogram from Figure 15a shows that different orientation of the grains gives different intensities. The set up for this experiment was sensitive for this for two reasons: (i) The amount of clay powder was very small. (ii) During measurement it was evident that the clay powder moved inside the glass capillary, both due to rotation of the capillary and the pressure put on the sample. The clay powder was elec-

trically charged and the small movement caused by rotation was amplified due to electrical repelling between the clay grains. This is a large source of error for the intensity. If the powder was more compressed at higher pressures, the intensity would increase due to larger amount of sample than for lower pressures.

The Fe(III)-FHT seemed to only have one distinct state for CO_2 adsorption, as no other peaks around the 001 peak were observed during pressurization.

5.1.2   Fe(III)-FHT-sim

The XRD of Fe(III)-FHT-sim from Figure 17 showed clear higher order peaks which indicate a very high degree of order in the sample. The drying process from Figure 18 showed a decrease in d-spacing of 5.27 Å which indicate the presence of 2 WL. Additionally, Figure 18 shows the total swelling due to CO_2 was 0.55 Å. The observed double peak showed that there was not intercalation of CO_2 molecules in all interlayers.

Figure 19 reveal that the CO_2 uptake in Fe(III)-FHT-sim was a slow process and the uptake was not as fast as it was for Fe(III)-FHT. The swelling for FHT with pressurized CO_2 can vary substantially: Hemmer et al. showed that the swelling process for Na-FHT took 9 days before the swelling ceased [12]. Medel et al. showed that anhydrous smectite (Wyoming montmorillonite) cation exchanged with Cs^+ gave a rapid adsorption of CO_2 [15]. The intensity sensitivity of the experimental setup was discussed above and may have caused sudden drops in intensity, as seen at approximately 60 min and 160 min. However, the general trend was that both intensity and d-spacing increased during the exposure of CO_2. This indicate that the uptake of each interlayer increases. Figure 20 emphasizes the observation of a slow equilibrium process of swelling due to CO_2 uptake in the interlayers of Fe(III)-FHT-sim. It should not be interpreted as an immediate uptake of CO_2 after 40 min. The seemingly abrupt change in d-spacing after 40 min only showed that the relative intensity from the double peak became higher for the low q top than for the high q top. Additionally, the nonswelling of the high q top can be seen from 0-40 min and the swelling of the low q top can be seen from 40-180 min. It is possible that the swelling would have continued further if the sample had been kept at 40 bar for a longer period of time.

5.1.3   Sources of error

This part of the discussion, for XRD at ESRF, will emphasize the sources of error. As mentioned earlier, the rotation of the sample meant the powder

moved inside the capillary. Glasswool fibers were also visually seen among the clay powder inside the capillary and could interfere with the result. The empty capillary that was filled with CO_2 and glasswool showed there is little change in the intensity for regions with small differences in q-vector. Therefore the glasswool is not considered any problem. For the drying process the cryostream did not warm all parts of the clay simultaneously and is the main reason for the difficulty of drying the Zn-FHT, Mg-FHT, Cu-FHT, Ni-FHT and Mn-FHT samples. Continues scanning across the sample with the cryostream was tried, but did not give successfully drying either. The Fe(III)-FHT and Fe(III)-FHT-sim was considered dry, i.e only iron hydroxides were left in the interlayer with no waterlayers. A better drying process would have been to dry all of the powder simultaneously and kept on drying after the bragg peak remained stationary. This was not possible at the ESRF as it would have been too time consuming for the beamtime that was given. The beamtime was also the main reason that Fe(III)-FHT-sim was not measured for longer than 3 hours.

Compared to other studies the pressure steps for Fe(III)-FHT were shorter in time than other similar studies, Hunvik et al. spent 2 hours at each pressure step [14]. A possible source of error is that the step did not reach its equilibrium before the next step was initiated. The heating process after CO_2 exposure is a clear example of this. The heated Fe(III)-FHT after CO_2 exposure was brought to 423 K without any temperature steps, but instead as a linear temperature increase. As the Figure 13 shows, the d-spacing of the exposed clay shrank at 326 K. Unfortunately, the lowest temperature at which CO_2 completely leaves the interlayer is unknown, because equilibrium at the different temperatures was not reached. This temperature is interesting for potential carbon capture usage as it effects the energy usage of the method. This should be investigated more thoroughly.

5.1.4 D8 Focus

The D8 focus and ESRF sample gave 11.24 Å and 10.74 Å for the 001 bragg peak for dried Fe(III)-FHT sample which is a difference of 0.5 Å. This shows that the drying process for interlayer water is better when vacuum is pumped on the sample with a short drying process compared to a much longer drying process and without pumping vacuum. This was again shown for the drying of Fe(III)-FHT-sim which gave a d-spacing difference of 1 Å.

The D8 Focus showed a minor shoulder for the 001 peaks of Fe(III)-FHT (Figure 23). The seemingly larger shoulder for the dry sample is caused by the overlapping background peak at 10.5 Å. However, the background should be equal for dry and wet sample and there is a shoulder for the wet peak. Therefore, the observed dry 001 peak shoulder is probably a

combination of both the background and the sample itself. If there is slighty more interlayers with cations than with cation hydroxides, there would be a minor shoulder/peak observed at the left side of the 001 bragg peaks.

The observed peak between 11.24-10.74 Å indicates a random inter-stratification, because the d-spacing match the expected d-spacing of the Fe(III) cation and hydroxide.

All the Fe(II)-FHT-sim & -pre and Fe(II)-FHT-pre gives promising d-spacing interlayer for CO_2 uptake. These samples should also be investigated further with a vacuum drying process and pressured CO_2. This will also provide information about the diffusion of water in to the interlayer upon cooling, which the D8 focus does not provide.

The wide 001 peak of Fe(II)-FHT-sim is probably caused by two different cation exchange processes, which give rise to two overlapping peaks.

The increased intensity for lower d-spacing peaks for the Fe(II)-FHT-sim and Fe(III)-FHT-sim compared to the -pre samples indicates that adding the cation salt solution after the clay and water gives a more amorphous clay structure.

The linear increase in background for increasing d-spacing (starting at 15 Å) is caused by the small angle between the source and detector ($2\theta < 6$ deg). As the angle increase ($2\theta > 6$ deg) the intensity background decreases. This is clearly seen as it is the common background for measurements done with and without the dome holder.

5.2 TGA

The results of Figure 26 showed that only Cu-FHT, Mn-FHT, Zn-FHT and Mg-FHT took up water at 323 K when cooled. Cu-FHT, Mn-FHT and Zn-FHT also took up water at 373 K, but at a lower rate. This may seemingly be in contrast to what was discovered at the ESRF X-ray measurements as only Fe(III)-FHT did not show a d-spacing change when cooled. However, the XRD measures the interlayer spacing of the clay sheets and therefore only give information about the presence of coordinated and interlayer water. In contrast, the TGA measurement measures the weight of vaporized: free water, interlayer water, coordinated water and water molecules previously adsorbed in the clay surface. This is important to emphasize before comparing the results. Therefore, there is no contradiction between the results if the samples showed no weight change when cooled or heated, but the interlayer swelled (hydrated) when cooled down. The TGA can not measure water diffusing in/out of the interlayer and out/in to the mesopores, as there is no weight change for this process.

As seen in Figure 26 the 6 hours of drying at 423 K were not enough

time to completely dry all the samples except Cu-FHT. Fe(III)-FHT, Mn-FHT, Mg-FHT, Zn-FHT and Ni-FHT did not reach constant mass at the end of the 423 K heating step and are therefore not considered dry. If there is still water present in the clay it can diffuse into the interlayer.

Fe(III)-FHT continued to dry for all the different temperature steps and does not take up water at 323 K, even after drying at higher temperature beforehand. The XRD measurement also showed that water did not easily reenter the interlayer of the Fe(III)-FHT. However, this result raise doubts if the Fe(III)-FHT sample measured at ESRF was completely dry. The criteria for a dry sample was that the peak position remained stationary upon cooling, but for Fe(III)-FHT this may not suffice. Additionally, the picture of Fe(III)-FHT from Figure 27 showed that there were clearly a visible darkening of the clay when the sample were dried. Figure 16b have a color gradient which shows that not every part of the sample were completely dried.

The other samples also gave a color change when dried, as seen in Figure 27 and this was not seen during the XRD measurement and drying at ESRF, which confirms again that the samples were not successfully dried. That dried clays give darker color turns out to be a visual phenomena which occur for all the samples and appear to be partially reversible (not for Ni-FHT).

The second heating process up to 573 K, seen in Figure 28 and 29 revealed other characteristics than the first heating process: The first weight loss of 6.7% for Cu-FHT correspond to what is expected for the loss of one WL (theoretical 7.5%). The mass loss of 3.2% commencing at the T_d temperature has been assigned dehydroxylation of the interlayer Cu hydroxide. Both the mass loss percentage and the decomposition temperature strongly indicate that this is a dehydroxylation process. The presence of a dehydroxylation process also shows that there is only one WL present in the interlayer after exposure to a 43% relative humidity atmosphere.

Ni-FHT also has a loss of 1 WL after a weight loss of 7.7% (theoretical 7.6%) and a subsequently dehydroxylation process 4.3% (theoretical 3.6%). In contrast to Cu-FHT the dehydroxylation process does not happen directly after the removal of one WL, but the processes are separated with approximately 110 K. The dehydroxylation process happens from 473-573 K which is similar to what has been observed by Hunvik et al. for Ni-FHT [33].

Zn hydroxide has the lowest decomposition temperature of the exchanged cations. The more complex TGA curve of Zn-FHT may be caused by the temperature at which water leaves the clay is very close to the T_d

of Zn hydroxide and therefore the processes overlap. The total mass loss could be caused by dehydration of a combination of mesopouros water, coordinated water and dehydroxylation. The expected mass loss from 1WL and dehydroxylation process is 11.1% and the remaining 3% are therefore caused by mesoporuos water. It seems that the dehydroxylation does not happen exactly at the temperature given for Zn hydroxide, but as the hydroxide inside the clay is not solid hydroxide there is expected some deviation.

The Mn-FHT first had a weight loss of 12.4% at 300-425 K. This weight loss is assigned to the loss of mesopouros water and 1 WL of coordinated water. Both Zn-FHT and Mn-FHT have been assigned mesopouros water in contrast to Cu-FHT and Ni-FHT. One would expect to see a difference in mass loss rate between the temperature at which loss of mesopouros and coordinated water occur. However, the location of the mesopouros water can be different for the different clay samples and therefore evaporate at temperatures closer or further apart from the temperature at which 1 WL evaporates. For Mn-FHT the temperature at which different types of water leaves the clay seems to be closer to each other than for Zn-FHT. The second mass loss of 1.9% have more inconclusive explanation. The T_d for Mn hydroxide is unknown and the mass loss is lower than expected for a dehydroxylation process. From comparison with the behavior of the other samples, the mass loss may be due to dehydroxylation process.

Fe(III)-FHT have a T_d of 500 K and the measured mass loss is caused by the evaporation of mesopouros water and 1 WL, measured at 4.6% and 9.4%. The expected mass loss of 2 WL for Fe(III)-FHT is 13.1% and could also be a possible explanation, if the sample contain little mesopouros water. Additionally, the XRD data shows that there are 2 WL present in the Fe(III)-FHT sample. However, the first heating process had a total mass loss of 17.5%, which clearly shows that there is large amount of uncoordinated water in the Fe(III)-FHT sample. The exposure of 43% RH also should give the sample a higher amount of mesopouros water than for the first heating process. The second heating process shows a lower mass loss than the first heating process for Fe(III)-FHT. This indicates that the drying process was better at 423 K for 6 hours than heating the sample to 573 K for a short amount of time.

Mg-FHT sample did show a mass loss of 4% and 7.4% between 300-400 K. They are assigned mesopouros water and coordinated water, respectively. The last mass loss of 1.9% between 450-490 K follow the same argument as for the dehydroxylation of Mn-FHT sample. The difference being that the T_d temperature of Mg-FHT is known and is at 653 K. A possible explanation is the similarity of hydration energy of Zn, Mg, Cu,

Mn and Ni (see Table 2), which all have been assigned a dehydroxylation process below 573 K.

The weight loss of Fe(III & II)-FHT-sim & -pre have all been attributed mesopouros water and 1 WL. The temperature at which the first weight loss for each Fe-FHT sample ends, is also indicative of the similar manner in which water leaves the Fe-FHT samples. There is no clear dehydroxylation step for any of the Fe-FHT samples. The low decomposition temperature and the similar hydration energy of Fe(II) compared to the other samples raises doubt about whether the decomposition of Fe(II)-hydroxide takes place or not. Fe(II)-hydroxide can decompose in several ways depending on the accessibility of oxygen and water [37]. If Fe(II)-oxide is produced from decomposition of Fe(II)-hydroxide, it can easily react in some way that is unclear and perhaps not give the weight loss of between 3-4% as in a normal dehydroxylation process [37].

Similar TGA measurements done by Mendel et al. (montmorillonite) and Mansa et al. (bentonite) also attributed the first mass loss to the loss of mesopouros water [15, 40]. Additionally, Mendel et al. also assign the last weight loss step for their clay samples to be dehydroxylation of the interlayer cations [15].

Fe(II)-FHT-pre and Fe(III)-FHT-pre take up water after drying and is probably caused by a more amorphous sample.

The global minima of the derivative for each sample could be a good indication of the temperature at which water leaves the clay the fastest. However, there are some effects that should be taken into account. The temperature could be lower than the measured temperature as there might be some delay in the system. The temperature measurement is outside the cruicible and therefore the actual temperature inside the sample could be lower than the measured temperature, even though this would only be a few degrees. The other effect is that the clay has a finite quantity of water and therefore the rate goes down as the clay is emptied for water. Therefore water would possible leave the clay faster at a higher temperature, but there is no more water which can leave at this temperature.

Some sources of errors that should be emphasized: The presence of mesopouros water is not taken into the theoretical calculations of the expected mass loss, but as the amount of mesopouros water is measured between 0-5% and therefore would not alter the expected weight loss by more than 0.5% and as the calculations have a higher uncertainty than 0.5%, this is not considered any problem.

The TGA has a horizontal furnace and it is unknown if the thermal expansion on the length of the balance-arm is corrected for. The short changes

of mass between the different temperature regimes from Figure 26 could indicate that this is not corrected for. There is a weight peak when heating and a weight valley when cooled, which agrees with the explanation of a non-corrected thermal expansion/contraction. A heating rate at 10 K/min was used in the first heating process, where this effect was observed. The temperature therefore exceeded the desired temperature with about 5 K for a minute before settling at the desired temperature and could perhaps contribute to the weight gain/loss observed at each heating step in Figure 26.

6   Conclusion

In the current study, the dried Fe(III)-FHT powder exhibited intercalation of CO_2 at a pressure of 18 bar. The swelling persisted within the pressure range of 0 to 50 bar, leading to a notable increase of 0.47 Å in the interlayer distance. Importantly, this intercalation phenomenon proved to be reversible upon heating the sample, as the basal spacing of the clay reverted to its dried state at a temperature of 423 K. There is a strong likelihood that the clay may exhibit reversible intercalation even at lower temperatures.

Fe(III)-FHT-sim exposed to 40 bar CO_2 exhibited a swelling of 0.55 Å after 3 hours and give promising results that more clay samples may be useful as a carbon capturing method if one can detect possible slow absorption processes.

Different cation exchanged fluorohectorites showed a large variation in water amount 6.7-16.2% at 43% RH. The interlayer hydroxides were dehydroxylated for Cu-FHT, Ni-FHT and Zn-FHT at the expected decomposition temperature. Mg-FHT showed a decomposition temperature 70 K above the expected temperature. The Fe(II & III)-FHT -sim & -pre did all show promising drying at 423 K. Additionally, the drying process with the use of vacuum was superior to remove WL from the hydroxides in the interlayer. Fe(II & III)-FHT-pre were more amourphous and subsequently showed an increased ability to take up water at 298 K.

[1]   A. Busch et al.'On sorption and swelling of CO2 in clays'. Geophys. 23 March 2016;vol.2:111-130.

[2]   K. W. B. Hunvik, K. K. Seljelid, D. Wallacher, A. Kirch, L. P. Caval-canti, P. Loch, P. M. Røren, P. H. Michels-Brito, R. Droppa-Jr, K. D. Knudsen, C. R. Miranda, J. Breu and J. O. Fossum, 'Intercalation of co2 selected by type of interlayer cation in dried synthetic hectorite,' *Langmuir*, vol. 39, no. 14, pp. 4895–4903, 2023.

[3]   J. Konta, 'Clay and man: Clay raw materials in the service of man,' *Applied Clay Science*, vol. 10, no. 4, pp. 275–335, 1995.

[4]   S. Lee and R. Tank, 'Role of clays in the disposal of nuclear waste: A review,' *Applied Clay Science*, vol. 1, no. 1, pp. 145–162, 1985.

[5]   K. hunvik et al., 'Co2 adsorption enhanced by tuning the layer charge in a clay mineral,' *LANGMUIR*, vol. 37, no. 49, pp. 14 491–14 499, 2021.

[6]   World Meteorological Organization, State of the Global Climate 2022 (WMO-No. 1316), 2023.

[7]   Al-Ghussain, L. (2019), Global warming: review on driving forces and mitigation. Environ Prog Sustainable Energy, 38: 13-21.

[8]   National Aeronautics and Space Administration. Sea Level [Internet]. USA: NASA; 2023 Feb [updated 2023 June 9; cited 2023 June 11].Available from: https://climate.nasa.gov/vital-signs/sea-level/.

[9]   European commision. Consequences of climate change [Internet].EU; [cited 2023 June 11].Available from: https://climate.ec.europa.eu/climate-change/consequences-climate-change$_e n$..

[10]   McBean, G. Climate Change and Extreme Weather: A Basis for Action. Natural Hazards 31, 177–190 (2004).

[11]   M. McNutt, 'Climate change impacts,' *Science*, vol. 341, no. 6145, pp. 435–435, 2013.

[12]   H. Hemmen, E. G. Rolseth, D. M. Fonseca, E. L. Hansen, J. O. Fossum and T. S. Plivelic, 'X-ray studies of carbon dioxide intercalation in na-fluorohectorite clay at near-ambient conditions,' *Langmuir*, vol. 28, no. 3, pp. 1678–1682, 2012.

[13]   L. michels et al., 'Intercalation and retention of carbon dioxide in a smectite clay promoted by interlayer cations,' *Scientific Reports*, vol. 5, no. 8775, pp. 1–9, 2015.

[14]   K. W. B. Hunvik, P. Loch, L. P. Cavalcanti, K. K. Seljelid, P. M. Røren, S. Rudić, D. Wallacher, A. Kirch, K. D. Knudsen, C. Rodrigues Miranda, J. Breu, H. N. Bordallo and J. O. Fossum, 'Co2 capture by nickel hydroxide interstratified in the nanolayered space of a synthetic clay mineral,' *The Journal of Physical Chemistry C*, vol. 124, no. 48, pp. 26 222–26 231, 2020.

[15]   N. Mendel, D. Sîretanu, I. Sîretanu, D. W. F. Brilman and F. Mugele, 'Interlayer cation-controlled adsorption of carbon dioxide in anhydrous montmorillonite clay,' *The Journal of Physical Chemistry C*, vol. 125, no. 49, pp. 27 159–27 169, 2021.

[16]   T. Nordvik (20.12.22) Intercalation of CO2 in Cation Exchanged Flourohectorite, in-depth study TFY4520.

[17]   Tubiana M. Wilhelm Conrad Röntgen et la découverte des rayons X [Wilhelm Conrad Röntgen and the discovery of X-rays]. Bull Acad Natl Med. 1996 Jan;180(1):97-108. French. PMID: 8696882.

[18]   S. Borisov and N. Podberezskaya, 'X-ray diffraction analysis: A brief history and achievements of the first century,' *Journal of Structural Chemistry*, vol. 53, Dec. 2012. DOI: `10.1134/S0022476612070013`.

[19]   J. J. Thomson M.A.F.R.S. (1897): XL. Cathode Rays , Philosophical Magazine Series 5, 44:269, 293-316.

[20]   M. Lederman, 'The early history of radiotherapy: 1895–1939,' *International Journal of Radiation Oncology*Biology*Physics*, vol. 7, no. 5, pp. 639–648, 1981, ISSN: 0360-3016. DOI: `https://doi.org/10.1016/0360-3016(81)90379-5`. [Online]. Available: `https://www.sciencedirect.com/science/article/pii/0360301681903795`.

[21]   A. A. Bunaciu, E. gabriela Udriştioiu and H. Y. Aboul-Enein, 'X-ray diffraction: Instrumentation and applications,' *Critical Reviews in Analytical Chemistry*, vol. 45, no. 4, pp. 289–299, 2015.

[22]   Kittel C. Introduction to Solid State Physics. 8th ed. New Jersey: John Wiley & Sons; 2005.

[23]   M.F. Brigatti, E. Galán, and B.K.G. Theng. "Chapter 2 - Structure and Mineralogy of Clay Minerals". In: Handbook of Clay Science. Ed. by Faïza Bergaya and Gerhard Lagaly. Vol. 5. Developments in Clay Science. Elsevier, 2013, pp. 21–81.

[24]   M. Brito et al. 'Unmodified Clay Nanosheets at the Air–Water Interface' Langmuir. Dec 2020;vol.37.

[25] Greenhouse Gases and Clay Minerals: Enlightening Down-to-Earth Road Map to Basic Science of ClayGreenhouse Gas Interfaces. eng. Green Energy and Technology. Cham: Springer International Publishing, 2018.

[26] E. dos Santos et al., 'Ciprofloxacin intercalated in fluorohectorite clay: Identical pure drug activity and toxicity with higher adsorption and controlled release rate,' *Royal Society of Chemistry*, vol. 7, no. 5, p. 26 537, 2017.

[27] J. Madejova, 'Ftir techniques in clay mineral studies,' *Vibrational Spectroscopy*, vol. 31, no. 1-10, 2003.

[28] M. W. Möller et al. 'Tailoring Shear-Stiff, Mica-like Nanoplatelets' ACS Nano. 2010;vol.4:717-724.

[29] Joshua Halpern. 8.2: Atomic and Ionic Radius. [Internet]. Cited 2022 Dec 06. Available from: `https://chem.libretexts.org/Courses/Bellarmine_University/BU%3A_Chem_103_(Christianson)/Phase_3%3A_Atoms_and_Molecules_-_the_Underlying_Reality/8%3A_Periodic_Trends_in_Elements_and_Compounds/8.2%3A_Atomic_and_Ionic_Radius`.

[30] A.G. Blackman. SI chemical data. Seventh edition. National Library of Australia:John Wiley Sons Australia Ltd;2014.

[31] L. F. Garcia-Herrera. "Thermogravimetric analysis"[Internet].LibreTexts;2022 Aug 22 [cited 2023 Mar 1] Available from:`https://chem.libretexts.org/Courses/Franklin_and_Marshall_College/Introduction_to_Materials_Characterization__CHM_412_Collaborative_Text/Thermal_Analysis/Thermogravimetric_analysis_(TGA)`.

[32] E. Palomba et al.'A -Thermogravimeter for Investigation of Volatile Compounds in Planetary Environments'. Orig Life Evol Biosph. 15 July 2015;vol46:273–281.

[33] P. L. et al., 'Spontaneous formation of an ordered interstratification upon ni-exchange of na-fluorohectorite,' *Applied clay Science*, vol. 198, p. 105 831, 2020.

[34] Q. Song, Z. Tang, H. Guo and S. Chan, 'Structural characteristics of nickel hydroxide synthesized by a chemical precipitation route under different ph values,' *Journal of Power Sources*, vol. 112, no. 2, pp. 428–434, 2002, ISSN: 0378-7753.

[35] T. SATO, S. IKOMA, F. OZAWA and T. NAKAMURA, 'Thermal decomposition of magnesium hydroxide,' *Gypsum Lime*, vol. 1982, no. 181, pp. 283–289, 1982.

[36] J. R. Günter and H. R. Oswald, 'Topotactic electron induced and thermal decomposition of copper(II) hydroxide,' *Journal of Applied Crystallography*, vol. 3, no. 1, pp. 21–26, Feb. 1970.

[37] N. Brett, K. MacKenzie and J. Sharp, 'The thermal decomposition of hydrous layer silicates and their related hydroxides,' *Quarterly Reviews, Chemical Society*, vol. 24, no. 2, pp. 185–207, 1970.

[38] N. Loganathan, G. M. Bowers, A. O. Yazaydin, H. T. Schaef, J. S. Loring, A. G. Kalinichev and R. J. Kirkpatrick, 'Clay swelling in dry supercritical carbon dioxide: Effects of interlayer cations on the structure, dynamics, and energetics of co2 intercalation probed by xrd, nmr, and gcmd simulations,' *The Journal of Physical Chemistry C*, vol. 122, no. 8, pp. 4391–4402, 2018.

[39] P. R. Jeon, J. Choi, T. S. Yun and C.-H. Lee, 'Sorption equilibrium and kinetics of co2 on clay minerals from subcritical to supercritical conditions: Co2 sequestration at nanoscale interfaces,' *Chemical Engineering Journal*, vol. 255, pp. 705–715, 2014, ISSN: 1385-8947.

[40] 'Preparation and characterization of novel clay/scleroglucan nanocomposites,' *Applied Clay Science*, vol. 126, pp. 235–244, 2016, ISSN: 0169-1317.

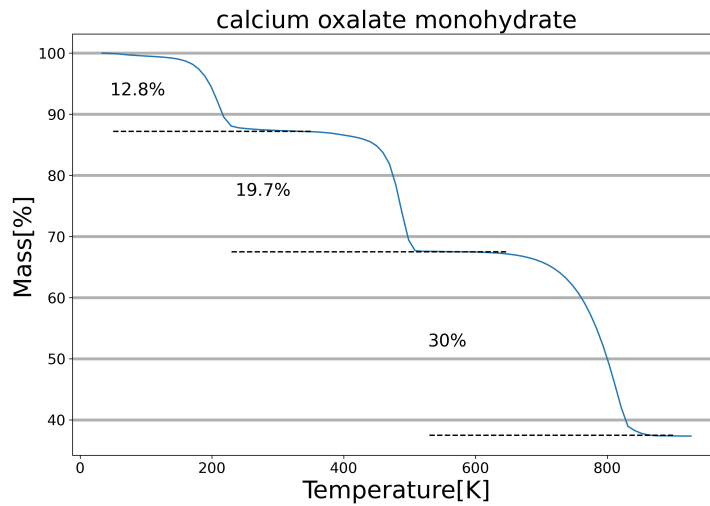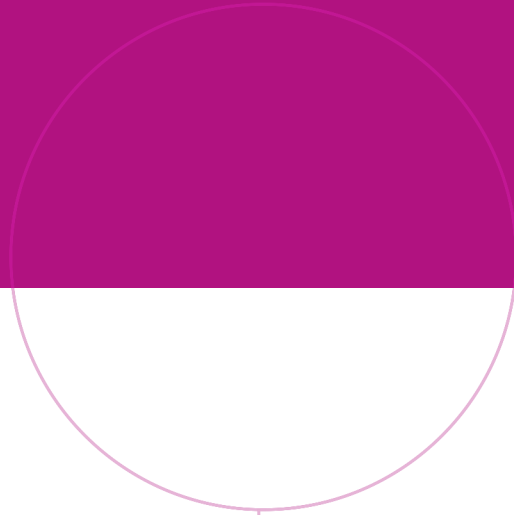# A   Calibration with calcium oxalate monohydrate

Figure 34: TGA calibration with calcium oxalate monohydrate. The weight loss for the different steps were 12.8%, 19.7% and 30%.

23 mg of calcium oxalate monohydrate powder was used to check the calibration of the TGA. Figure 34 shows the percentage weight loss for the three steps for calcium oxalate monohydrate. The steps gave a weight loss of 12.8% (see chemical reaction 7), 19.7% (see chemcial reaction 8) and 30% (see chemical reaction 9) with the theoretical value of 12.3%, 19.2% and 30.1%, respectively. The deviation is considered low when compared to the theoretical data.